

Study Of Decoherence Effects In Cold Atom Optical Lattices

Andreas Blendl

Masterarbeit in Physik
angefertigt im Physikalischen Institut

vorgelegt der
Mathematisch-Naturwissenschaftlichen Fakultät
der
Rheinischen Friedrich-Wilhelms-Universität
Bonn

01/11 2019

I hereby declare that this thesis was formulated by myself and that no sources or tools other than those cited were used.

Bonn,
Date

.....
Signature

1. Gutachter: Prof. Dr. Dieter Meschede
2. Gutachter: Prof. Dr. Simon Stellmer

Contents

1	Introduction	1
2	Theory	3
2.1	Optical lattices	3
2.1.1	Oscillator model	3
2.1.2	Light shifts and optical potentials	5
2.2	State dependent polarization synthesized optical lattice for cesium	6
2.3	Decoherence effects in optical lattices	8
2.3.1	Population relaxation time T1	9
2.3.2	Coherence relaxation time T2	9
3	Measurement Techniques	13
3.1	Loading an ensemble of atoms into the optical lattice	13
3.2	Bloch Sphere representation of the qubit	14
3.3	Measure qubit transition frequency	16
3.4	Ramsey interferometry	17
4	Measurements	19
4.1	Feed forward magnetic-field stabilisation	19
4.1.1	Current stabilisation	19
4.1.2	Magnetic feed forward stabilisation	21
4.1.3	Atomic stabilisation	22
4.2	Investigation of coherence time	23
4.2.1	Decoherence due free fall Ramsey interferometry	23
4.2.2	Estimate of decoherence due to magnetic field noise measurement	33
5	Conclusion and outlook	41
	Bibliography	43
A	Useful information	47
A.1	Characterisation of fluxgate magnetometer	47

Introduction

Atomic physics is booming and advancing at a quite rapid pace. Major development in light-sources such as the Ti:Sa [1], which can be tuned over a broad frequency domain (670 - 1070 nm), or diode lasers [2] and fiber lasers has pushed research topics in the past few decades. Shaping short pulses at the fs regime was enabled by the Ti:Sa and Kerr-lens mode-locking [3]. The concept of laser cooling made regimes as μK and nK reachable [4], by evaporative cooling [5] pK regimes became reachable and lead to the realisation of a Bose Einstein Condensate [6]. It became the leading field for high precision measurements in the timekeeping area defining the second by a cesium fountain clock [7]. Nowadays even fractional precision of 10^{-18} is reachable [8]. Quantum simulators are reaching out to explore new Hilbert-spaces.

One type of quantum simulators can be realized by optical lattices. Paving the way to quantum cellular automata [9], delivering a highly controllable quantum system, which can be used to simulate and study new Hilbert-Spaces. By the creation of entangled states in optical lattices, quantum computation can be explored.

The research presented in this thesis is related to the field of quantum computation and quantum information processing. The experiment conducted in this thesis is making use of the existence of a *magic – wavelength* for alkali-atoms, a one dimensional polarization-synthesized state-dependent optical lattice [10] has been implemented. The apparatus is capable of performing state dependent transport of cold ^{133}Cs atoms. By the use of external driving fields, as microwave or raman-pulses, the internal states of atoms can be manipulated. This allows to carry out shift (spatial displacement) and coin (rotation of the internal state) operations. By using this operations, discrete-time quantum walks can be realized [11], testing the non-classical, ballistic spread of a massive particle in time and thereby testing the Leggett-Garg-inequality using negative measurements [12]. In addition to that using this system, a massive particle interferometer could be implemented, carrying out a quantum Hong-Ou Mandel measurement [13]. Since the system is a periodically time-driven quantum system, it is a Floquet system. By studying the topology of discrete-time quantum walks, novel topologically-protected edge states occurring in Floquet topological insulators can be investigated [14]. Carrying out the above mentioned experiments relies on being able to perform multiple shift and coin operations under coherent control of the apparatus. To extend the number of coin and shift operations, two different approaches can be carried out. One is to carry out the measurement much faster than the apparatus coherence time and the other one is to extend the coherence time of the apparatus.

When aiming to improve the coherence time of the apparatus, an in depth investigation of the apparatus limits in terms of coherence time has to be carried out. Former investigation lead to the classification of two different decoherence effects: spin and spatial decoherence. In addition, the apparatus is effected by

spin decoherence rather than spatial decoherence [15].

This thesis is a study of the decoherence mechanisms effecting the apparatus. A feed forward magnetic field stabilisation is presented, aiming at the reduction of magnetic field noise. Furthermore, the dephasing due to magnetic field noise is classified as homogeneous, by carrying out homogeneous dephasing insensitive Ramsey interferometry. During the process of this thesis an analysis technique was developed to investigate the dephasing due to transition frequency fluctuations of the implemented qubit on the example of magnetic field noise. Revealing a full understanding and prediction of the coherence due to the investigated noise source. As an outlook for further investigations a post correction for magnetic field noise effecting the apparatus is presented, indicating a limit for future magnetic field stabilisations.

Theory

2.1 Optical lattices

Optical lattices became one of the working horses in atomic physics research. It is now a well studied and understood framework in cold atomic physics and thereby subject of several review articles [16, 17] and is still providing a rich playground in the field of atomic physics.

The mechanism of an optical dipole force acting as a trapping potential was first considered theoretically by Askar'yan (1962) and Letokhov (1968). The first optical dipole trap was realised later by Chu et al. (1968) [18].

The core of the apparatus is the realisation of a state-dependent polarization synthesized optical lattice, therefore a brief insight in the physics behind optical dipole traps or in other words optical lattices is given. Optical lattices rely on the atomic electric-dipole interaction. The physics can be understood classical in an Oscillator model. The dipole force arises from the dispersive interaction of the induced atomic dipole moment with the intensity gradient of the light field. The minima of the light potential can then be used as a trapping potential. By making use of far-detuned laser light, absorptive dipole-interaction is dominated by the dipole force acting on the atom. The absorptive dipole-interaction gives rise to photon scattering and sets a limit to the performance of dipole-traps. Since the interaction is very weak typical trap depth are in the microkelvin regime.

2.1.1 Oscillator model

Assume an atom placed in an electric field (in most cases generated by a Laser). The electric field \vec{E} induces an atomic dipole moment \vec{p} oscillating at frequency ω . The amplitude of the atomic dipole moment is then related to the amplitude of the electric field by.

$$\vec{p} = \alpha \vec{E}$$

With $\alpha(\omega)$ the complex polarizability. This interaction gives rise to an interaction potential of the form

$$U_{\text{dip}} = -\frac{1}{2} \langle \vec{p} \vec{E} \rangle = -\frac{1}{2\epsilon_0 c} \text{Re}(\alpha) \cdot I \quad (2.1)$$

In a straight forward manner a conservative induced dipole force follows

$$F_{\text{dip}}(r) = -\nabla \cdot U_{\text{dip}}(r) = \frac{1}{2\epsilon_0 c} \text{Re}(\alpha) \nabla \cdot I(r)$$

The power absorbed by the oscillator is then given by

$$P_{\text{abs}} = \langle \dot{p} \vec{E} \rangle = 2\omega \text{Im}(\tilde{p} \tilde{E}^*) = \frac{\omega}{\epsilon_0 c} \text{Im}(\alpha) \cdot I(r)$$

The absorption power can be interpreted as photon scattering in cycles of absorption and subsequent spontaneous emission. A scattering rate can therefore be calculated by:

$$\Gamma_{SC} = \frac{P_{\text{abs}}}{\hbar\omega}$$

This expression is valid for any particle in an oscillating electric field. Out of the Lorentz-Oscillator-Modell, where the atom is assumed as an electron being bound elastically to the core with an eigenfrequency ω_0 , an expression for the polarizability α can be found, by integrating the equation of motion. In this model, damping results from the power radiated by an accelerated charge, expressed in Larmor's formula (see [19]).

$$\alpha(\omega) = 6\pi\epsilon_0 c^3 \frac{\Gamma/\omega_0}{\omega_0^2 - \omega^2 - i(\omega^3/\omega_0^3)\Gamma} \quad (2.2)$$

Using a semiclassical approach, where a quantized two level system interacting with a classical radiation field is assumed, the atomic polarizability can be calculated by the matrix dipole element between ground and excited state. In this case, it is assumed that saturation effects can be neglected. In this case Γ is given, by

$$\Gamma = \frac{\omega_0^3}{3\pi\epsilon_0 \hbar c^3} |\langle e|\mu|g\rangle|^2$$

For the D lines of alkali atoms the classical result agrees with the true decay rate to within a few percents. For strong driving, saturation effects start to play a role, and (eq.2.2) is no longer valid. In the case of dipole trapping, far-detuned light is used, leading to low saturation and therefore scattering rates ($\Gamma_{SC} \ll \Gamma$). Out of (eq. 2.1) and (eq. 2.2) and in the presence of large detunings and therefore low scattering rates, the expression for the dipole potential and the scattering rate can be derived.

$$U_{\text{dip}}(r) = -\frac{3\pi c^2}{2\omega_0^2} \left(\frac{\Gamma}{\omega - \omega_0} + \frac{\Gamma}{\omega_0 + \omega} \right) I(r), \quad (2.3)$$

$$\Gamma_{SC}(r) = \frac{3\pi c^2}{2\hbar\omega_0^3} \left(\frac{\Gamma}{\omega_0 - \omega} + \frac{\Gamma}{\omega_0 + \omega} \right)^2 I(r) \quad (2.4)$$

These equations show two resonances at $\omega = \omega_0$ and $\omega = -\omega_0$, in case of a close tuning of the driving frequency to the resonance frequency ω_0 , the famous 'rotating-wave approximation' applies and the counter-rotating term $\omega = -\omega_0$ can be neglected, since the detuning $\Delta = \omega - \omega_0$ is much smaller than ω_0 .

Then (2.3) and (2.4) reduce to

$$U_{\text{dip}}(r) = \frac{3\pi c^2 \Gamma}{2\omega_0^3 \Delta} I(r) \quad (2.5)$$

$$\Gamma_{SC}(r) = \frac{3\pi c^2}{2\hbar\omega_0^3} \left(\frac{\Gamma}{\Delta}\right)^2 I(r). \quad (2.6)$$

From these two expressions the connection between U_{dip} and Γ_{SC} can already be understood.

$$\hbar\Gamma_{SC} = \frac{\Gamma}{\Delta} U_{\text{dip}} \quad (2.7)$$

From (2.5) and (2.6) we can already understand two fundamental aspects for dipole trapping.

1. **Sign of detuning** : for red detuned driving frequency ω ($\Delta < 0$) the dipole potential becomes attractive since it has a negative sign. For a blue detuned driving frequency ω ($\Delta > 0$) the potential becomes repellent.
2. **Intensity and detuning** : whereas the dipole potential scales as I/Δ , the scattering rate scales as I/Δ^2 . To get an optimal tradeoff between trapping potential and scattering rate, it is common to run dipole traps at large detuning and high intensities.

2.1.2 Light shifts and optical potentials

The energy shift of a two level atom subset to far-detuned laser light can be understood by describing the interaction of the laser light with the atom as a time-independent perturbation in second order of the electric field. For non-degenerate states the interaction Hamiltonian H_1 leads to an energy shift of the i -th state

$$\Delta E_i = \sum_{j \neq i} \frac{|\langle j | H_1 | i \rangle|^2}{E_i - E_j} \quad (2.8)$$

Where E_i is the unperturbed energy of the i -th state. The summation is carried out over all atomic states $i \neq j$, whose transition energy is close to $\hbar\omega$ (the field energy per photon), contributions from energy states far away are suppressed by the denominator. The interaction Hamiltonian H_1 is given by the electric dipole operator $\boldsymbol{\mu} = e \cdot \mathbf{r}$. For a two-level atom the energy shift of the ground state E_i simplifies to

$$\Delta E = \pm \frac{|\langle e | \boldsymbol{\mu} | g \rangle|^2}{\Delta} |E|^2 = \pm \frac{3\pi c^2 \Gamma}{2\omega_0^3} \frac{\Gamma}{\Delta} \cdot I \quad (2.9)$$

This result reveals an interesting aspect. The optically induced energy shift (known as 'light shift' or 'ac Stark shift') for the ground state corresponds to the dipole potential for the two-level atom and has opposite sign as the excited state.

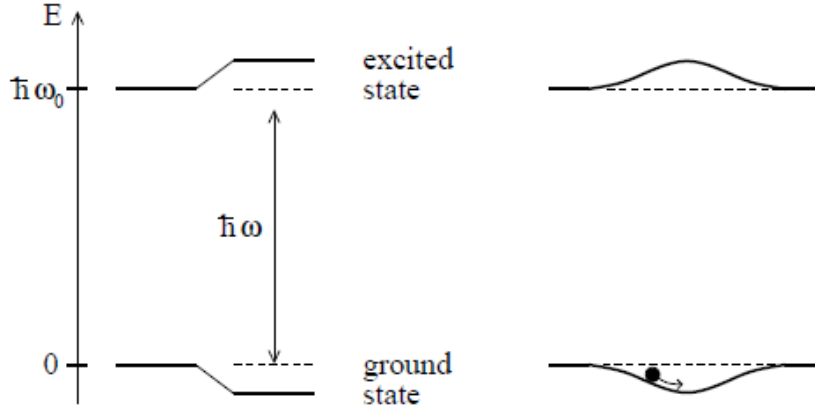


Figure 2.1: (Left-hand side) Light shifts for a two-level atom for red-detuned light. (Right-hand side) Spatially inhomogeneous laser beam produces a potential well in which an atom can be trapped, taken from [17].

2.2 State dependent polarization synthesized optical lattice for cesium

Aiming to have a system which is capable of storing a quantum qubit and provide spatial and state control an apparatus which can deliver a state selective control over the implemented qubit is needed. This desired claim is fulfilled by a state dependent optical lattice which can be regarded as the evolution of a pure optical lattice, where no state selective control of the trapped atoms is possible.

The first realisations of state dependent optical lattices have been suggested by Deutsch and Jaksch [20, 21]. They have become a nowadays widely used investigation tool in cold atomic physics and still deliver a rich investigation platform.

The conceptual idea is to spatially overlap two optical dipole traps and in an ideal case address with each of them different internal states of the trapped atom. This conceptual idea can be understood in a quantum mechanical treatment which takes into account the AC vector polarizability, where the dipole interaction between the atom and the light field takes into account the sum over all possible internal transitions (see 2.1.2).

For cesium a nearly 'magic wavelength' $\lambda_{DT} = 865.9$ nm can be found in which this situation is nearly fulfilled [13, 22].

The two outermost long lived hyperfine states $|3, 3\rangle$ and $|4, 4\rangle$ of cesium are utilised, where an atom in the $|3, 3\rangle$ is predominantly attracted by σ^- light and an atom in the state $|4, 4\rangle$ is only attracted by σ^+ light. Identify the two states as a qubit, which can be coupled by microwave radiation at 9.2 GHz. Thereby a two-level system is identified as $|\downarrow\rangle := |3, 3\rangle$ and $|\uparrow\rangle := |4, 4\rangle$. A more intuitive understanding of the generation of our state dependent lattice can be achieved by only studying the fine structure associated to the $^2S_{1/2}$ ground state. In this case the following spin states are identified as a qubit system:

$$|\uparrow'\rangle = |J = 1/2, m_J = +1/2\rangle \quad (2.10)$$

$$|\downarrow'\rangle = |J = 1/2, m_J = -1/2\rangle \quad (2.11)$$

There is a wavelength λ_{DT} which is simultaneously red detuned to the D_1 line ($^2S_{1/2} \rightarrow ^2P_{1/2}$) and blue detuned to the D_2 line ($^2S_{1/2} \rightarrow ^2P_{3/2}$), where $\lambda_{D1} = 894.592$ nm and $\lambda_{D2} = 852.347$ nm [23]. An atom in the state $|\uparrow'\rangle$ effectively feels no potential from σ^- light since it is exactly the same amount red detuned from the D_1 line as it is blue detuned from the D_2 line and therefore the potentials cancel out exactly for σ^- light induced transitions (vice versa for the $|\downarrow'\rangle$ state).

Unfortunately it is not possible to map the hyperfine qubit system onto the fine structure. Performing a basis transformation from the hyperfine to the fine structure yields our qubit states:

$$|\uparrow\rangle = |I = 7/2, m_I = 7/2\rangle \otimes |\uparrow'\rangle \quad (2.12)$$

$$|\downarrow\rangle = \sqrt{\frac{7}{8}} |I = 7/2, m_I = 7/2\rangle \otimes |\downarrow'\rangle - \sqrt{\frac{1}{8}} |I = 7/2, m_I = 7/2\rangle \otimes |\uparrow'\rangle \quad (2.13)$$

The resulting potentials are therefore given by

$$U_{\uparrow} = U_{\sigma^+} \quad (2.14)$$

$$U_{\downarrow} = \sqrt{\frac{7}{8}} U_{\sigma^-} - \sqrt{\frac{1}{8}} U_{\sigma^+} \quad (2.15)$$

While the $|\uparrow\rangle$ state is in second order insensitive to the electric field of the σ^- light this does not apply to the $|\downarrow\rangle$ state. From eq. 2.14 and 2.15 one can understand, that the spatial position of an atom in $|\uparrow\rangle$ is determined by the motion of its corresponding trapping lattice σ^+ (σ^-), therefore giving rise to a state dependent lattice. In this apparatus a novel scheme of spin-dependent transport based on a high precision, large bandwidth synthesizer of polarization states of light, is used. Further information about the experimental setup, can be found in [13, 24].

The optical dipole trap is formed by two spatially overlapped and counter-propagating Gaussian laser beams ($\lambda_{DT} = 866$ nm) which are focussed to a waist $\omega_{DT} = 17$ μ m inside a ultra high vacuum glass chamber. Along the longitudinal direction the formed potential arises out of the interference of the two counter-propagating laser beams, resulting in a $\cos^2(k_{DT} \cdot x)$, with k the wavevector. The formed potential can be seen and treated as a defect free one dimensional crystal of light with lattice constant $a_{DT} = \frac{\lambda_{DT}}{2} = 433$ nm.

In the transverse direction the potential is directly given by the focussed Gaussian beam profile. Therefore the potential is given by

$$U(x, \rho) = U_0 \frac{\omega_{DT}^2}{\omega(x)^2} e^{-\frac{2\rho^2}{\omega(x)^2}} \cdot \cos^2\left(\frac{2\pi}{\lambda_{DT}} x\right) \quad (2.16)$$

Where ρ is the transverse position, x the longitudinal position, $\omega(x)$ the gaussian waist at position x and U_0 the maximum potential depth. The curvature of the wavefront and the Guy phase of the Gaussian beams can be neglected, since the number of occupied lattice sites spreads over a distance which is one order of magnitude smaller than the Rayleigh length of our focussed Gaussian beam.

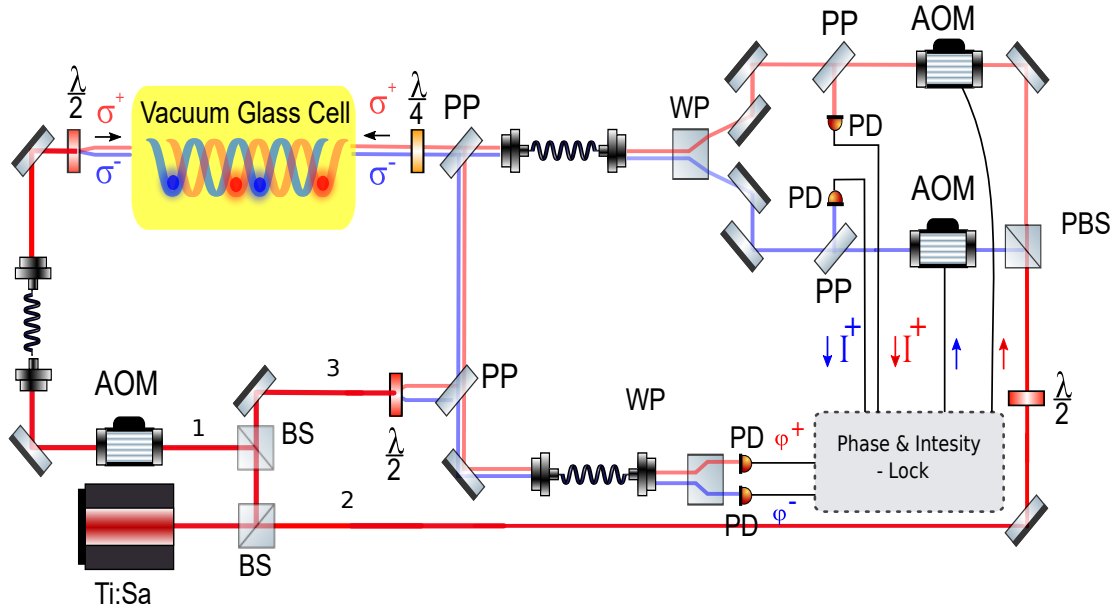


Figure 2.2: Setup of the generation of the synthesized optical lattice. The Ti:Sa is generating the optical lattice beam at $\lambda_{Ti:Sa} = 865.9$ nm and 2.5 mW maximum power. Using two beam splitters (BS) the beam is split into three parts. Beam (1) is split using a $\lambda/2$ -plate and a polarization beam splitter into its two circular polarization components (σ^+ and σ^-) and is counterpropagated by beam (3), forming the two standing wave potentials creating the optical lattice in the vacuum glass cell. Each of the two polarization arms of beam (1) is steered by an acousto-optical-modulator (AOM) and is later overlapped via a Wollaston prism to form one propagation arm of the optical lattice. After the AOMs the intensity of each polarization arm is measured by extracting a small portion of the light and measure the intensity via a Photodiode (PD). To achieve a measure of the phase of the two components of beam (1) it is mixed with the bare laser beam (2) generating a beating signal, which is measured in each polarization arm, extracting a portion of the light using a pickup plate (PP) and measure the intensity using a photo diode (PD). The phase lock is realised by steering the frequency of the AOM signal. The intensity lock is obtained by steering the amplitude of the AOM signal, using an electronic phase and frequency lock-box. For simplicity the intensity lock of beam (3) is omitted.

experimental Setup

2.3 Decoherence effects in optical lattices

Since the implemented off resonant optical lattice is built to perform experiments revealing quantum statistics, it is necessary to deal with a coherent quantum state. Thus it is interesting to take a look at the mechanism that lead to decoherence in the implemented qubit state.

When talking about decoherence, two different effects have to be distinguished. The first effect is a decay of the population of the implemented qubit state, the associated lifetime is described by the T1 time. A brief discussion of the T1 time of the implemented qubit in this apparatus will be given in 2.3.1.

The second effect leading to decoherence is due to a spatial or temporal varying qubit transition frequency.

2.3.1 Population relaxation time T1

The relaxation rate of neutral atom's hyperfine levels has been studied intensely. For example, the realisation of the first Bose Einstein Condensate [25] has been prevented due to spin relaxations from elastic collisions in a Magneto Optical Trap. Due to the spatial separation of neutral atoms, trapped in an optical dipole potential, spin relaxations caused by elastic collisions do not deliver the dominating physical effect. The dominating effect leading to a population relaxation in an optical dipole potential has been measured to be given by off resonant scattering of lattice photons[26, 27]. The population decay of a spin 1/2 system can be described by an exponential decay [28].

$$P_{\uparrow}(t) = P_{EQ} - P_{EQ} \cdot e^{-\frac{t}{T1}} \quad (2.17)$$

Where P_{EQ} denotes the equilibrium population between the \uparrow / \downarrow state and T1 the time of a $1/e$ decay. The relaxation time in this apparatus has been extensively studied and has revealed a relaxation time $T1 = 92 \pm 12$ ms [13]. For a pure spin 1/2 system the equilibrium population P_{EQ} is given by 1/2. This is not the case in the situation of the implemented qubit, since atoms can potentially scatter to any cesium hyperfine sublevel. It has been shown that in the case of cesium atoms in a linearly polarized lattice with a parallel quantization axis $P_{EQ} = 7/16$ [17], in the present apparatus P_{EQ} has been measured to be at $P_{EQ} = 39 \pm 2\%$. The discrepancy between the measurement and theoretical value is assumed to have its origin in the applied measurement technique, where only the population in one sublevel is measured. The measured T1 time gives a hard boundary on the long term perspective of state dependant transport of cesium, since there are only two possible tuning parameters to lower the off-resonant scattering of lattice photons. It is possible to lower the dipole potential and a change of the lattice-wavelength can be carried out. Where in the case of a change of the lattice potential wavelength a state dependent transport will be prevented.

2.3.2 Coherence relaxation time T2

The core of this apparatus is the implementation of a state dependant optical lattice. As this experimental tool enables to study a broad spectrum of experiments, it comes with the cost of a higher coupling of environmental effects to the implemented qubit. While inelastic scattering events lead to a population decay, as already discussed in sec 2.3.1, elastic scattering events lead to a loss of coherence due to the different height of the probability amplitudes of the implemented qubit state. More classically speaking elastic scattering events lead to a loss of coherence due to a spatial or temporal varying qubit transition frequency. When aiming to quantify the effects, leading to a decay of the coherence relaxation time T2, the associated phase variance of the qubit transition frequency can be used.

In the following a discussion of the physical origins of the decay of the coherence relaxation time T2 will be given, taken from [15].

Differential light shift lead to a shift of the transition frequency of the implemented qubit.

Due to their temperature distribution, atoms which are loaded into the optical lattice experience different spatial positions. As a reason different trapping potentials result, assuming a frozen position during the interrogation time. Each atom experiences a different shift of the transition frequency leading to inhomogeneous broadening. The energy shift an atom experiences is proportional to

$$\Delta E = |\eta|U/\hbar \quad (2.18)$$

Where η denotes the differential light shift and U the potential energy the atom experiences due to its position in the lattice. η is taking into account the distribution of a scalar and a vectorial light shift $\eta = \eta_v \cdot \epsilon + \eta_s$. Where ϵ is given by the degree of ellipticity of the light polarization, reflecting the imbalance of the I_{\pm} intensity components of σ^{\pm} polarized light

$$\epsilon = \frac{I_+ - I_-}{I_+ + I_-} \quad (2.19)$$

The scalar effect η_s was modelled by Kuhr et al [29] and can be described by

$$\eta_s = \Delta_{HF} \left(\frac{3}{2\Delta_{D1} + \Delta_{D2}} - \frac{1}{\Delta_{D1}} - \frac{1}{\Delta_{D2}} \right) \quad (2.20)$$

Where Δ_{HF} is given by the hyperfine splitting between the $|\uparrow\rangle$ and $|\downarrow\rangle$ state. The vectorial effect was modelled by Steffen et al [24] and can be described by

$$\eta_v = [m_F(\uparrow)g_F(\uparrow) - m_F(\downarrow)g_F(\downarrow)] \frac{\Delta_{D1} - \Delta_{D2}}{2\Delta_{D1} + \Delta_{D2}} \quad (2.21)$$

Where Δ_{D1} and Δ_{D2} describe the detuning of the lattice to the D1 and D2 line of cesium, $m_F(s)$ the magnetic quantum number of the corresponding spinstate s and $g_F(s)$ the corresponding g-factors. In the apparatus at hand the scalar light shift accounts to $\eta_s = 2.5 \cdot 10^{-3}$ and $\eta_v = 7/4$. An estimate of the corresponding coherence time $T_2 = 2\hbar/(|\eta|k_B T)$ of $T_2 \approx 600\mu s$ has been found for the scalar effect and $T_2 \approx 1\mu s/|\epsilon|$ has been found for the vectorial effect. For this estimate a transverse temperatur of $T_{2D} \approx 10\mu K$. Where the definition for the inhomogeneous coherence time T_2 has been taken from [29]. A measurement of the stress induced birefringence has found values for ϵ on the order of $\epsilon \approx 10^{-2}$ revealing a coherence time of $T_2 = 100\mu s$.

Fluctuations of the lattice depth originating from beam pointing instabilities and fluctuations of the optical lattice laser beams intensity. It has to be differentiated between common mode intensity fluctuation of the two lattice polarizations $I_{cm} = (I_+ + I_-)/2$ and relative fluctuations $I_r = I_+ - I_-$. Common mode fluctuations lead to a varying scalar differential light shift. The contrast $c(\tau)$ can be obtained out of the phase variance which is determined by the relative intensity spectral density

$$\Delta\Phi^2(\tau) = \frac{\tau^2 \eta_s^2 U_0^2}{\hbar^2} \int_0^\infty d\omega \text{sinc}^2(\omega\tau/2) RIN(\omega) \quad (2.22)$$

Where U_0 is given by the potential depth at the bottom of the optical potential.

Relative intensity fluctuations lead to a varying vectorial light shift. Here the the phase variance can be obtained from the noise spectral density of the ellipticity $\epsilon = I_r/(2I_{CM})$

$$\Delta\Phi^2(\tau) = \frac{\tau^2 \eta_v^2 U_0^2}{\hbar^2} \int_0^\infty d\omega \text{sinc}^2(\omega\tau/2) S_\epsilon(\omega) \quad (2.23)$$

Due to the fact that $\eta_v \gg \eta_s$ relative differential light shifts have a more severe impact on the decoherence.

Uniform magnetic field fluctuations lead to a homogeneous shift of the transition frequency of atoms loaded into the optical lattice and therefore to homogeneous dephasing. Magnetic field fluctuations originate ones from noise in the driving current of the coils generating the quantization field and external magnetic fields. The phase variance can be obtained out of the noise spectral density along the

quantization axis.

$$\Delta\Phi^2 = \frac{\tau^2 \mu_B^2}{\hbar^2} [m_F(\uparrow)g_F(\uparrow) - m_F(\downarrow)g_F(\downarrow)]^2 \int_0^\infty d\omega \text{sinc}^2(\omega\tau/2) S_B(\omega) \quad (2.24)$$

Magnetic field gradient fluctuations produce the same shift of transition frequency but contributes to spatial decoherence, which lead to inhomogeneous dephasing, due to its position dependence. The effect of magnetic gradient field fluctuations is assumed to be order of magnitude smaller than uniform magnetic field fluctuations due to the assumption that the separation of the atoms to the noise sources is orders of magnitude smaller than the separation of the atoms inside the optical lattice.

Information on more decoherence sources, such as motional excitations during atomic transport, fluctuations of the lattice position or spontaneous scattering of lattice photons can be found in [15].

Measurement Techniques

In this chapter, experimental techniques are described and further explained. There will be an explanation on how an atomic ensemble is loaded into the optical lattice and how the transition frequency of the qubit is measured as well as how Ramsey spectroscopy can be performed, which is used as a measurement tool for coherence.

3.1 Loading an ensemble of atoms into the optical lattice

Since the trapping potentials of the optical lattice are very weak ($\max \approx 370 \mu\text{K}$), it is not sufficient to load atoms into the optical lattice directly from the background vapour of the vacuum glass cell. The pressure inside the vacuum cell is at around 10^{-9} mbar [13] leading to an average velocity 200 ms^{-1} , assuming a boltzman-distributed velocity of the atomic cloud. To load an ensemble of atoms into the optical lattice, where it becomes accessible for further interrogation, the ensemble of atoms has to be precooled. The velocity is lowered using a Magneto Optical Trap (MOT). The principle of a Magneto Optical Trap has been well studied [30, 31] and it has become a well understood tool in experimental atomic physics.

The principle relies on slowing down atoms by radiation pressure. The absorbed photons are then isotropically emitted by the atoms, leading to a net impulse transfer to the atoms in the propagation direction of the laser beam. After scattering multiple photons, the atom is decelerated by the radiation pressure of the laser beam. Extending this principle to three dimensions this concept is referred to as optical molasse [32, 33]. By red detuning the laser beam slightly from the transition frequency of the atom, one exploits the doppler shift. Atoms counterpropagating the laser beam see the doppler shifted frequency of the laser which corresponds to their resonance frequency, leading to absorption of photons and deceleration. Making use of this technique a minimum temperature of $T_{\text{Doppler}} = 125 \mu\text{K}$ is achievable for cesium, even lower temperatures are possible with molasse cooling by making use of the multilevel structure of the ground state of alkali atoms and the laser polarization gradient [34]. Because of the absence of a position dependence force in a optical molasse, it is not possible to trap atoms. Atoms will diffuse out of the optical molasse.

To achieve a trapping potential, the concept of a optical molasses can be extended to a MOT. Therefore the optical molasse is extended with a magnetic quadrupole field which serves as magnetic field gradient and is giving rise to a position dependent lifting of the degenerate Zeeman sublevels. Similar to the principle of the doppler shifting in a optical molasse. In this situation either σ^+ or σ^- light will induce a transition depending on the position of the atom inside the magnetic field. Atoms will thus be trapped in the zero crossing of the magnetic field.

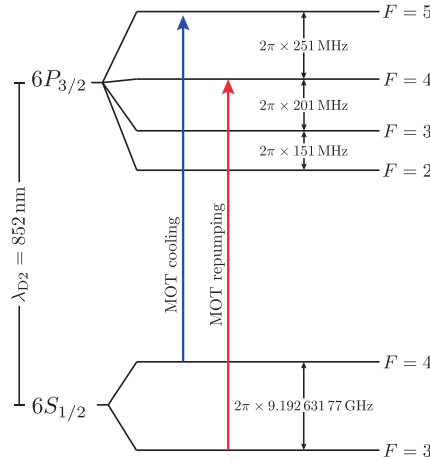


Figure 3.1: schematic picture of the implemented cooling transitions, taken from [13]

In the apparatus, the quadrupole magnetic field is generated by a pair of anti-helmholtz coils. The six optical molasse beams are produced by a single laser, split into six different beams tuned to the $|F = 4\rangle \rightarrow |F' = 5\rangle$ transition. This is a closed transition, due to the suppression of a decay to the $|F = 3\rangle$ state, which underlays the dipole selection rules.

Due to off resonant transitions to the $|F' = 4\rangle$ state, atoms can still decay into the $|F = 3\rangle$ state and in this case drop out of the cooling cycle. Employing a repumping laser for the $|F = 3\rangle \rightarrow |F' = 4\rangle$ transition, these atoms can be pumped back into the cooling cycle, shown in fig. 3.1.

Both lasers are self-built interference-filter-stabilized external cavity lasers that ensure stable single mode operation and a reduced linewidth (Gaussian linewidth $\Delta\nu < 10$ kHz).

3.2 Bloch Sphere representation of the qubit

To transfer the population of atoms initialized in the $|\uparrow\rangle$ state to the $|\downarrow\rangle$ state microwave, radiation is used in the measurements presented in this thesis. To prevent coupling to the other m_F sublevels a strong guiding field of $|B| = 3$ G is applied, inducing a spectral separation of consecutive m_F sublevels of 1.05 MHz [29]. The interaction of the microwave radiation and the dipole moment μ of the atom can be described by a semiclassical approximation. The wave function of an arbitrary superposition state between $|\uparrow\rangle$ and $|\downarrow\rangle$ can then be described by

$$|\psi\rangle = c_{\uparrow}|\uparrow\rangle + c_{\downarrow}|\downarrow\rangle \quad (3.1)$$

Where the complex amplitudes $|c_{\uparrow}|^2 + |c_{\downarrow}|^2 = 1$.

The optical bloch equations [35] apply in this situation to describe the dynamics of two level system. The optical bloch equations can be obtained by solving the Heisenberg equation of motion in the rotating wave approximation. Population and coherence relaxations can be introduced into the system as damping terms. The following set of partial differential equations can be derived

$$\left\langle \frac{\partial u}{\partial t} \right\rangle = \Omega_R(t) \sin(\phi_{MW}) \langle w \rangle + \delta \langle v \rangle - \frac{\delta \langle u \rangle}{T_2} \quad (3.2)$$

$$\left\langle \frac{\partial v}{\partial t} \right\rangle = \Omega_R(t) \cos(\phi_{MW}) \langle w \rangle - \delta \langle u \rangle - \frac{\delta \langle v \rangle}{T_2} \quad (3.3)$$

$$\left\langle \frac{\partial w}{\partial t} \right\rangle = -\Omega_R(t) \cos(\phi_{MW}) \langle v \rangle - \Omega_R(t) \sin(\phi_{MW}) \langle u \rangle \delta \langle v \rangle - \frac{\langle w \rangle - w_0}{T_1} \quad (3.4)$$

Where w describes the population, u and v the coherence of the qubit state, $\delta = \omega - \omega_0$ the detuning, $\Omega_R = \mu B \hbar$ the Rabi frequency of the driving field and ϕ_{MW} the phase of the driving field, which is in this these microwave radiation. T_1 denotes the population relaxation time and T_2 the coherence relaxation time.

With the use of the Bloch vector (u, v, w) , the temporal evolution of the implemented qubit can be visualized on the bloch sphere, see fig. 3.2. In case of perfect resonance $\delta = 0$ and no decoherence ($T_1 = T_2 = \infty$) the temporal evolution of the bloch vector can be analytically solved yielding

$$w(t) = -\cos(\Omega_R(t)) \quad (3.5)$$

For a chosen Rabi power field strength over a duration Δt it is therefore possible to precisely control the population of the implemented qubit. For a pulse area of $\int dt \Omega_R t = \pi$, the qubit state can be inverted $|\uparrow\rangle \rightarrow |\downarrow\rangle$, or brought into an equal superposition $|\uparrow\rangle \rightarrow \frac{1}{\sqrt{2}}(|\uparrow\rangle + |\downarrow\rangle)$ for a pulse area of $\pi/2$. By controlling the phase ϕ_{MW} a selection of the rotation axis of the Bloch vector is accessible, enabling the performance of Ramsey spectroscopy, see 3.4.

In the current experimental setup, it is possible to obtain a maximum Rabi frequency of 58 kHz. The envelope of the pulse can be shaped on timescales $> 20 \mu\text{s}$ by the additional use of an external trigger, rectangular pulses with a timing resolution of 100 ns can be achieved. More details about the experimental setup can be found in [36].

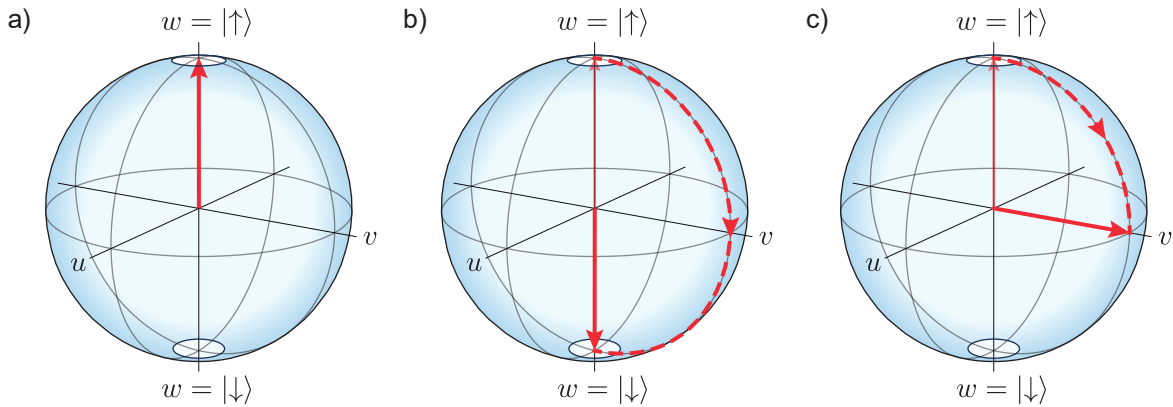


Figure 3.2: Bloch sphere representation of two-level system. a) $|\uparrow\rangle$ -state represented by the north pole b) drawing of a spin-flip $|\uparrow\rangle \rightarrow |\downarrow\rangle$ for a π -pulse. c) drawing of a $\pi/2$ pulse, creating an equal superposition of $|\uparrow\rangle$ and $|\downarrow\rangle$

3.3 Measure qubit transition frequency

Once the ensemble of atoms is loaded into the optical lattice, the number of atoms is determined. Illuminating the ensemble of atoms in the deep optical lattice ($370 \mu K$) using the optical molasse beams, produces fluorescence light of the atoms at $\lambda_f = 852 \text{ nm}$. The fluorescence light is collected using an electron multiplication CCD - camera¹ employed after a diffraction limited microscope ($NA = 0.29$). The number of atoms can be estimated by the integrated fluorescence light. After determining the number of atoms, F- and m_F pumping [37] is applied to transfer the population into the $|\uparrow\rangle$ state of our qubit. Further information can be found in [24]. To measure the qubit transition frequency of the implemented qubit the atomic ensemble is transferred to the $|\downarrow\rangle$ state. To transfer the population, an external driving field has to be applied. Microwave radiation is used to transfer the population, applying a pulse with a pulse area of π . The used addressing pulses in this thesis are fast rectangular pulses at the maximum microwave power available possible, to achieve a spectrally broad and fast transition. The effect of the Rabi-frequency on the spectral resolution is generally referred to as power-broadening [38]. In principle the spectral resolution of a microwave pulse can become infinitively narrow, but will be limited by the natural line width (100 Hz). As microwave radiation is homogeneous over the interrogation region, where atoms are trapped, a global population transfer is achieved. After applying an external driving field, the population of atoms is mapped onto the $|\downarrow\rangle$ and $|\uparrow\rangle$ states. The mapping is achieved by removing all atoms in the lattice in the $|\uparrow\rangle$ state. For removing the atoms a pushout technique is used, where a short resonant pushout beam is applied resonant to the $|4\rangle \rightarrow |5'\rangle$ line, removing all atoms in the $|\uparrow\rangle$ state, with an efficiency of 99%. The remaining atoms are counted, again via fluorescence imaging. A schematic drawing of the physical sequence, can be found in fig. 3.3. Repeating this measurement for different driving field frequencies, the population of transferred atoms versus the applied driving field frequency can be measured and the transition frequency extracted. Out of the obtained microwave spectrum, see (fig. 3.4) the transition frequency is extracted by carrying out a least squares fit. In the case of fig. 3.4 an analytic fit model is used, neglecting the effect of decoherence ($T_1 = T_2 = \infty$).

$$n = \frac{s \cdot \Omega_R^2}{\Omega_R^2 + (x - \delta)^2} \sin^2\left(\pi \sqrt{\Omega_R^2 + (x - \delta)^2} t_p\right) \quad (3.6)$$

Where s describes the survival and t_p the pulse length.

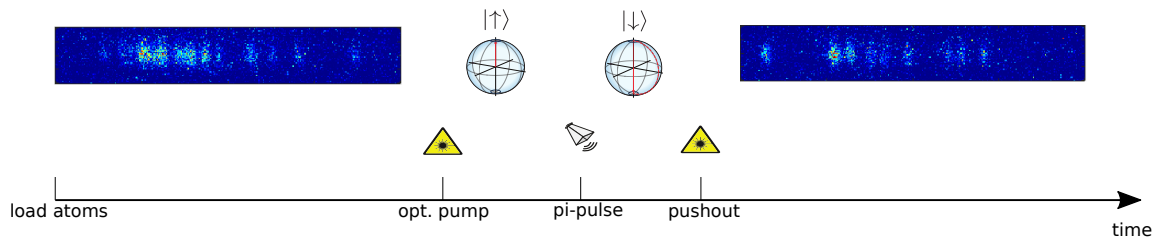


Figure 3.3: chronological physical sequence of a microwave spectrum.

¹ Andor: iXon DV897DCS-FI

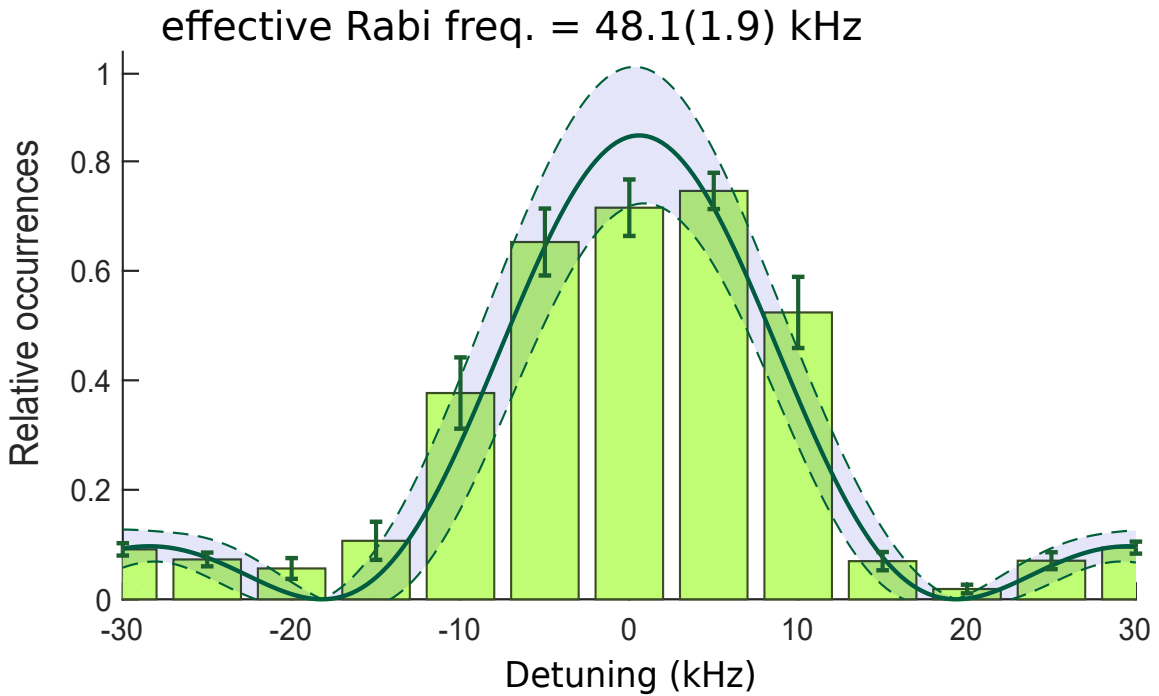


Figure 3.4: microwave spectrum for a square pulse with a pulse area of π and a pulse length of $10\mu s$. Since the spectrum has been measured in free fall, the number of relative occurrences does not reach 100% for resonance.

3.4 Ramsey interferometry

There are various approaches on how to carry out a Ramsey interferometry [39] measurement. The present apparatus allows to scan the phase of the microwave radiation and thus the rotation angle of the Bloch vector. The experimental procedure starts with the initialization of the ensemble of atoms in the $|\uparrow\rangle$ -state. After determining N_0 the number of atoms loaded, a first $\pi/2$ -microwave square pulse transfers the population into an equal superposition of $|\uparrow\rangle$ and $|\downarrow\rangle$. For a defined Ramsey time τ the atoms remain in this defined state. A second $\pi/2$ -microwave square pulse is applied, after a chosen Ramsey time τ . In the specific case of perfect resonance and no decoherence the second $\pi/2$ -pulse will transfer all remaining atoms in the $|\downarrow\rangle$ -state. When both microwave pulses have been applied, all remaining atoms are mapped to the $|\uparrow\rangle$ and $|\downarrow\rangle$ -state by removing all atoms in the $|\uparrow\rangle$ -state, using the afore mentioned pushout technique. The usual imaging technique is used to measure the number N_ϕ of the atoms to be in one of the two qubit states. A schematic drawing of the physical sequence can be found in fig. 3.5. Repeating the measurement routine, with different phases of the microwave radiation ϕ_{MW} from $[0, 2\pi]$, the rotation angle of the qubit can be scanned and a Ramsey fringe can be recorded. For a defined phase ϕ_{MW} of the qubit, a cosinus dependence between the number of relative occurrences $n = N_\phi/N_0$ and ϕ_{MW} is expected. Decoherence entering the apparatus, during the Ramsey time, will lead to a dephasing of the atoms in the equatorial plane of the Bloch sphere. In this situation the phase-match between ϕ_{MW} and the qubit is not well defined anymore. The obtained relative occurrences will become unrelated to ϕ_{MW} , leading to a decay of the amplitude of the cosinus dependence between n and ϕ_{MW} . Fitting a cosinus to the Ramsey fringes of the form

$$n = \frac{s}{2} (1 + c \cdot \cos(\phi_{MW})) \quad (3.7)$$

Where $c(\tau)$ defines the contrast and $s(\tau)$ the survival for a given Ramsey time τ . The contrast $c(\tau)$ delivers a quantitative measure for the coherence of the system for that particular Ramsey time. This measurement has to be repeated many times, in order to obtain a good statistical measure.

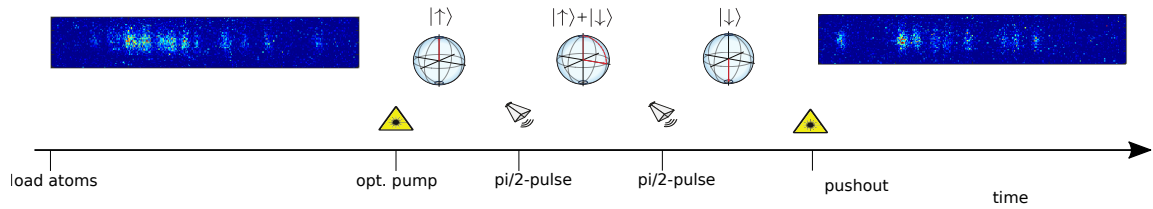


Figure 3.5: conceptual drawing of the physical sequence for carrying out Ramsey interferometry.

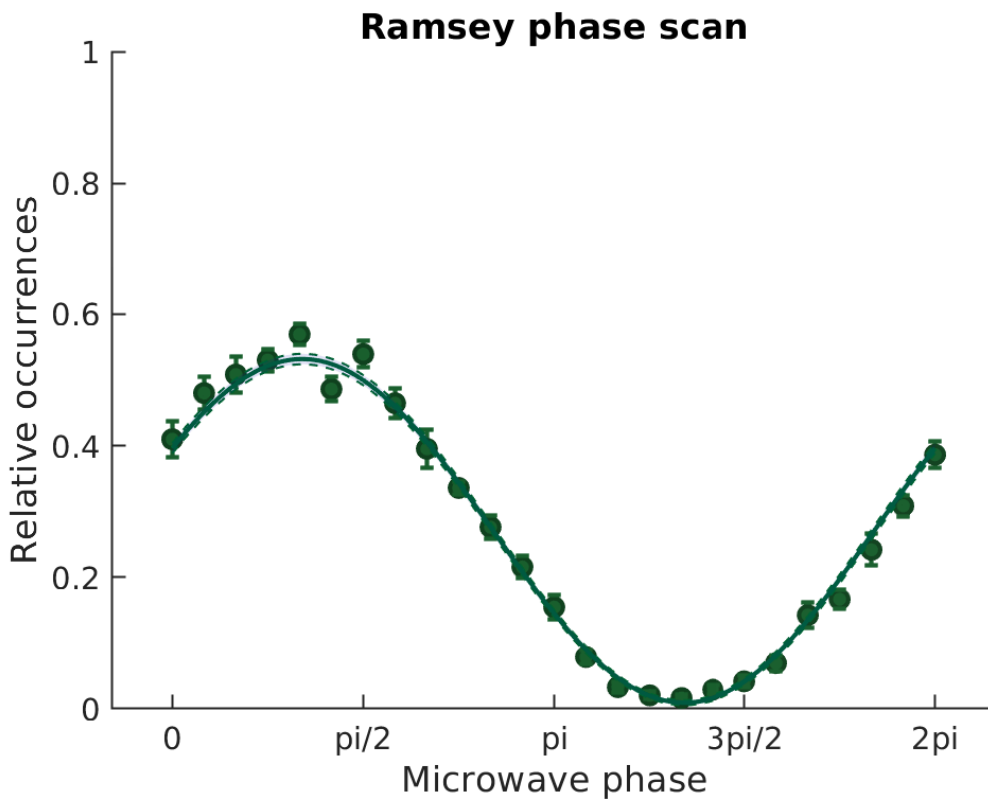


Figure 3.6: Ramsey fringe measurement for a Ramsey time of $1\mu s$ together with cosine fit, in free fall. The height of the amplitude of the cosine is limited by the survival.

Measurements

4.1 Feed forward magnetic-field stabilisation

The following chapter is based on the design and setup of a magnetic field stabilisation. Starting with a stabilisation of the driving current for the experimental coils, which are used to generate the quantization field, it will be reported about a magnetic field feed stabilisation as well as an atomic performance test of the feed forward stabilisation.

4.1.1 Current stabilisation

The goal of the current stabilisation is to suppress noise in the coil driving current by utilizing a proportional-integral-stabilisation-circuit. The current setup for the generation of the driving field is straight forward. The current is generated via a programmable toellner power-supply¹ providing a relative current stability $I_{\text{rms}}/I_0 = 10^{-5}$ on the relevant timescales. By further stabilizing the current in the driving circuit we aim to further diminish the dephasing produced by fluctuations in the driving current and on top of that pave the way to modulate the driving current and become able to compensate for external magnetic field noise in the vicinity of our atoms.

The principle of operation is as following, see fig 4.1. The current in the circuit is probed by measuring the voltage over a high precision resistor shunt², which has a very high thermal stability of $10^{-6} \frac{\Omega}{K}$. The voltage over the resistor is measured by an operational amplifier, which has a high common mode noise rejection, the generated voltage is then compared to a constant reference voltage, in case of no modulation, delivered by a high-precision voltage reference source³. The difference between the measured voltage at resistor and the voltage reference source is used as an error signal to steer a MosFet. In this way a proportional integrational circuit is applied. By steering the gate of the MOSFET⁴ its resistance is tuned, controlling the current running through the compensation coils.

The circuit is designed to be floating with respect to any ground potential. This setup ensures to break any potential ground loop generating noise. The performance of the stabilisation is tested by measuring the spectral noise power density using a spectrum analyzer⁵, figure 4.2. A suppression of the noise in the frequency domain up to 10 kHz is achieved, gaining up to one order of magnitude suppression for the lower frequencies. This also holds true, for the visible 50 Hz noise and higher harmonics, which stay

¹ Toellner TOE 8733-1

² Isabellenhuetten, AKZ-H2

³ High Precision 10V Reference, AD587

⁴ IRF520

⁵ HP 3589 A Spectrum/Network Analyzer

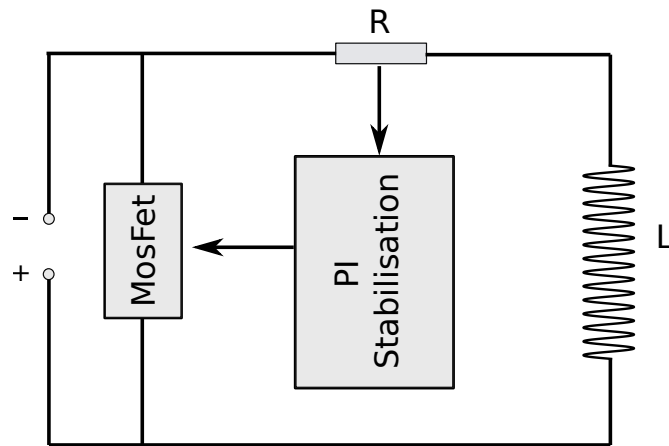


Figure 4.1: Schematic drawing of the current stabilisation circuit. The current is probed by a high precision resistor shunt and used as an in loop measurement of a proportional integral stabilizazation circuit. A MosFet serves as an actuator of the system. The resistance of the MosFet is varied by steering the gate of the MosFet with the servo signal of the stabilisation. Steering the resistance of the MosFet gives acces to steering the current in the coil driving circuit.

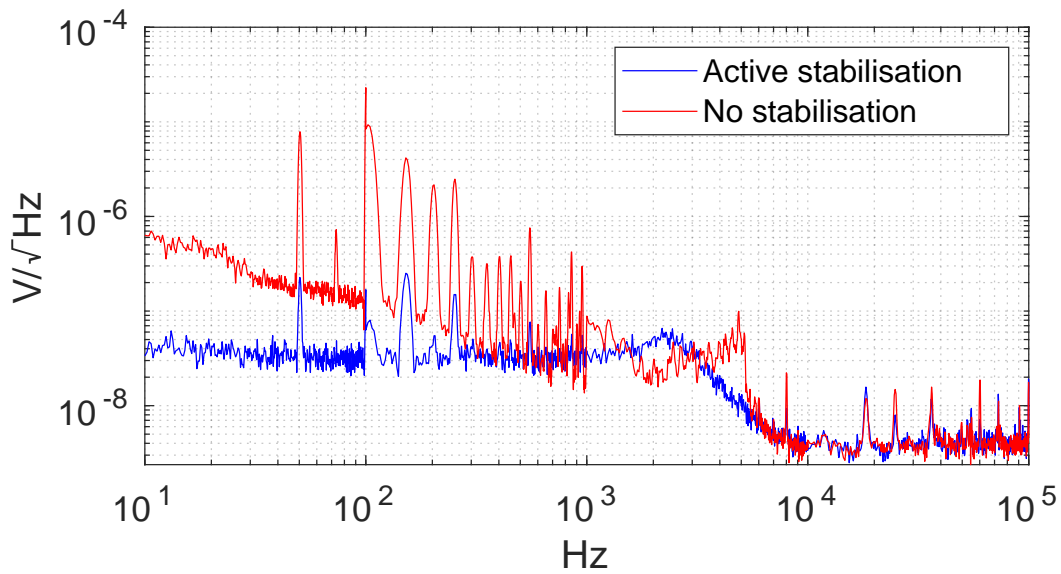


Figure 4.2: Spectral noise density of the current driving the experimental coils. In red without a stabilisation and blue with active stabilisation. The instrumental background has been from both measurements.

resilient in case of active compensation. In the frequency domain above 10 kHz no noise suppression is obtained, indicating the bandlimit of the stabilisation circuit. A measure of the step response, where the experimental coils have been replaced by a resistor with equivalent resistance, has been performed and yields a bandwidth of the electronic stabilisation circuit at 17 kHz. Whereas a measure of the step response, where the experimental coils are included, reveals a bandwidth of 2 kHz, indicating a boundary of any active magnetic field compensation using the magnetic coils producing the quantization field. A measure of the RMS noise of the driving current yields a more intuitive measure of the stability of the

driving current.

$$\frac{I_0}{I_{RMS}} = 10^{-6} \quad (4.1)$$

Whith $I_0 = 1.73$ A. Which results in fluctuations of the transition frequency of the implemented qubit < 100 Hz.

4.1.2 Magnetic feed forward stabilisation

Origins of external magnetic field fluctuations

To stabilise the transition frequency of the implemented qubit, it is necessary to compensate for external magnetic field fluctuations. External magnetic field fluctuations can be caused by several different sources. Electronic devices in the laboratory itself, produce magnetic fields mostly at frequencies of 50 Hz and higher harmonics. Transformers inside power supplies produce magnetic fields varying due to power line fluctuations at 50 Hz and higher harmonics. These fluctuations are assumed to be coherent in time, due to the stability of the 50 Hz noise in the power line. Triggering the apparatus to these kind of fluctuations ensures to have a time coherent system with respect to the noise originating from the power line ripple. These fluctuations are measured to produce a fluctuation of the transition frequency on the order of 10 kHz. On top of this, external magnetic fields produced from outside the laboratory lead to a transition frequency change on the order of 1 kHz (there might be statistical outliers). The origins of these fields reach out from other experiments in the building up to fluctuations of the earth magnetic field. Since external magnetic field fluctuations due to the line ripple lead to the biggest magnitude of transition frequency change a compensation of these field fluctuations was most promising.

Due to the property of time coherence concerning these kind of field fluctuations a feed forward compensation is possible and is implemented in the apparatus. In the following it will be reported about the setup and performance of a feed forward magnetic field compensation.

Principle of operation

The performance of the implemented feed forward magnetic field stabilisation is dominated by two different aspects. Once the stabilisation has an electronic limit and once the assumption of time coherent noise is crucial. The electronic limit of the stabilisation is given by the SNR of the measurement device as well as by the bandlimit of the stabilisation which is measured to be at 1 kHz. The SNR of the measurement device has also been measured and is on the order of 20 dB for up to 1 kHz. Since the measurement of the SNR of the measurement device was not trivial, an in detail description of the measurement routine can be found in the appendix [A.1](#). Due to the magnetic quantization field, the change of the qubit transition frequency produced by fields which are perpendicular to the quantization field are highly suppressed. Therefore it is sufficient to compensate magnetic field noise parallel to the quantization axis. As the fluxgate magnetometer is not exactly at the position of the atoms a scaling factor has to be found, accounting for the different magnetic field produced at the position of the sensor and at the position of the atoms due to the magnetic field lines produced by the compensation coils. Whereas the external magnetic field is assumed to be spatially homogeneous since its' origins are orders of magnitude further away than the separation of the fluxgate magnetometer to the actual position of the atoms.

It can be reported about an electronic stabilisation of the external magnetic field noise which lead to a transition frequency shift on the order of < 500 Hz at the position of the sensor. To test the stabilisation with an atomic level the transition frequency change is measured in time and the nonstabilised field is

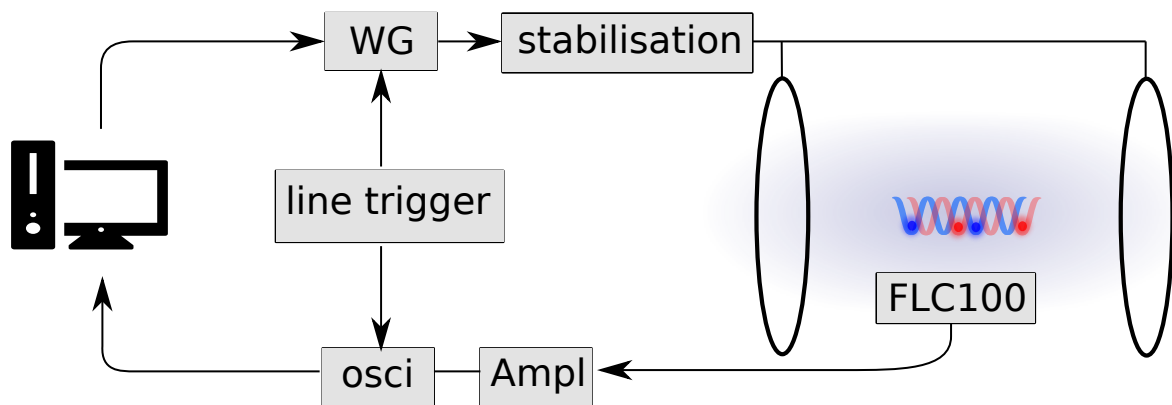


Figure 4.3: The magnetic field noise in the vicinity of the atoms is measured using a fluxgate magnetometer, aligned to the quantization axis. The signal is electronically amplified using a low noise high precision amplifier and bandfiltered using a RLC filter with a cutoff frequency of 2 kHz. Using an oscilloscope the signal is acquired synchronized to the line trigger extracted out of the power line ripple. Via a computer the read out of the oscilloscope is performed, where a softwarewise filtering is applied and a deconvolution with the transfer function of the stabilisation. Using a waveform generator the set point of the current stabilisation is modulated according to the recorded noise signal.

compared against the stabilised field.

4.1.3 Atomic stabilisation

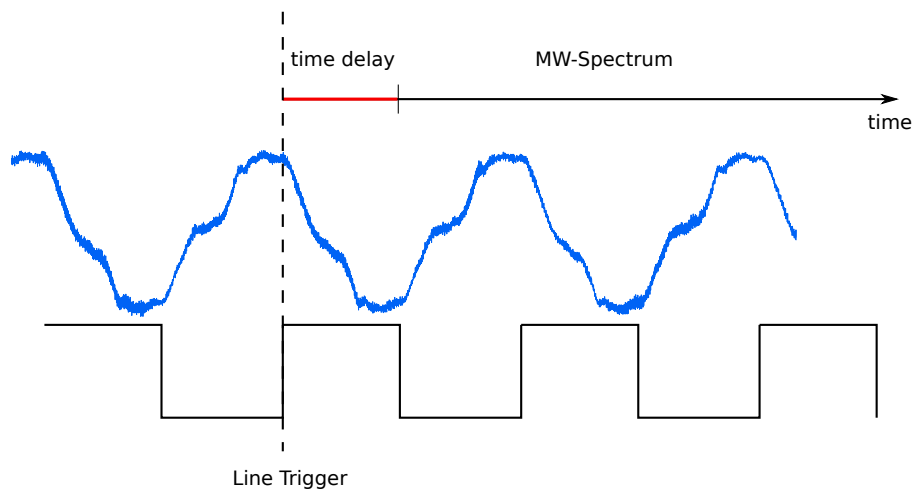


Figure 4.4: schematic picture of the experimental procedure to measure the qubit transition frequency in time. In blue the 50 Hz line ripple from which the line trigger is extracted. The experimental sequence is triggered with the rising edge of the line trigger. A variable delay is added with respect to the line trigger before recording a microwave spectrum.

To test the feed forward stabilisation on an atomic level, the change of the transition frequency is measured in time, once with an active feed forward stabilisation and once without active feed forward stabilisation. To extract the transition frequency a microwave spectrum using a square pulse with a length of $30 \mu\text{s}$ is recorded. A relatively long pulse length is chosen to gain a sharp spectral resolution in order to decrease the error on the extracted qubit transition frequency. A variable time delay is added in front

of the physical sequence to record a microwave spectrum which allows to measure the qubit transition frequency with respect to the phase of the 50 Hz noise. At this point it is necessary to keep in mind that the apparatus is synced to the 50 Hz line trigger. Therefore a variable time delay is added with respect to the 50 Hz line trigger. Choosing a time delay from 0 to 25 ms allows to observe the change of the transition frequency during one period of 50 Hz and test the performance of the feed forward magnetic field stabilisation with atomic precision.

Comparing the results (see fig. 4.5) a peak to peak fluctuation in the noncompensated case of about

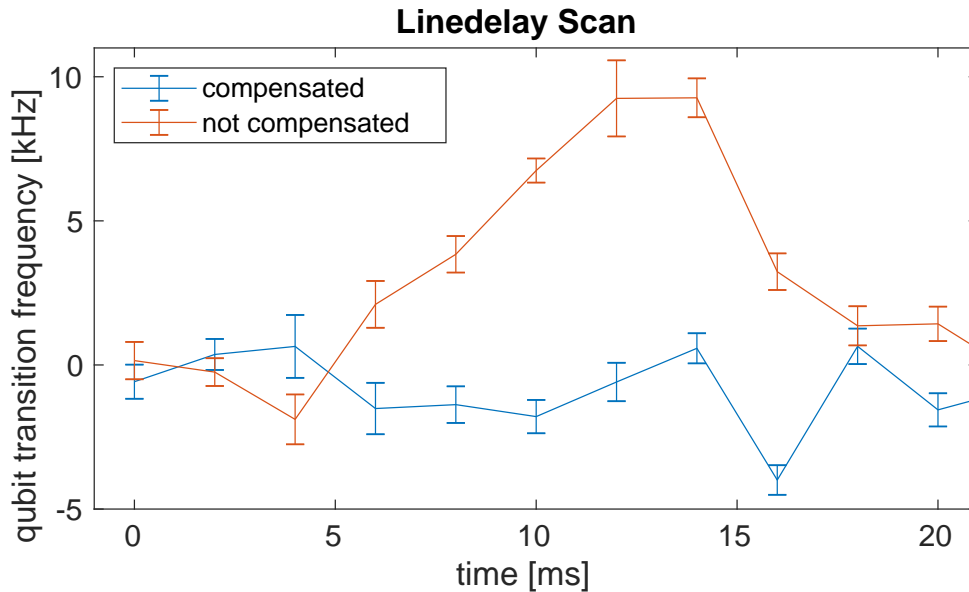


Figure 4.5: measurement of the qubit transition frequency with respect to the phase of the 50 Hz noise. In blue with an active feed forward compensation. In red without feed forward stabilisation.

10 kHz of transition frequency change is present, whereas a peak to peak fluctuation of about 4 kHz in the compensated case is present. Nevertheless this does not hold the promised electrical limit of the stabilisation of the transition frequency below 500 Hz. There are various effects that could potentially explain the limit of the stabilisation. For example a strong gradient in the external magnetic field between the position of the sensor and the atoms, nevertheless this is not very likely, since the separation is orders of magnitude smaller than the separation to the origin of the magnetic field noise. To explain the limit of a feed forward stabilisation in the present situation an in deep magnetic field noise analysis has been carried out in chapter 4.2, where low frequency (DC) magnetic field fluctuations on the order of kHz are found, explaining the limit of the stabilisation. In conclusion a feed forward magnetic field stabilisation aiming at 50 Hz noise and higher harmonics is not sufficient for the current situation of the apparatus.

4.2 Investigation of coherence time

4.2.1 Decoherence due free fall Ramsey interferometry

The aim is to obtain a quantitative measure for the decoherence effecting the qubit system. Measuring the temporal decay of bare Rabi - Oscillations cannot provide a good measure of the decoherence. They are not particularly sensitive to decoherence, because of the fact of dynamic de-coupling in Rabi-Oscillations [40, 41]. The most common way to measure the decoherence is by Ramsey interferometry 3.4. The aim

is to obtain a quantitative measure for the decoherence of the qubit state due to magnetic field fluctuations. This can be done by carrying out a Ramsey interferometry for different Ramsey times in free fall. For this purpose the lattice is turned off after the state preparation, leaving the atoms in free fall during the Ramsey time. Since the atoms are not spatially confined by the lattice potential they spread according to their temperature, leading to a loss of atoms for increasing Ramsey times. Due to the loss of atoms, different survivals occur, when measuring Ramsey fringes for different Ramsey times. It is accounted for that, by measuring independent survivals for every Ramsey time. Out of the evolution of the obtained contrast for increasing Ramsey times a quantitative measure of the apparatus coherence time can be obtained. The coherence relaxation time T_2 is defined as the time, when the contrast has reduced to 50 %.

Statistical contrast analysis

Starting from the analytic expression for a Ramsey fringe, eq 3.7. The relative occurrences $n = \frac{N_{\phi_{MW}}}{N_0}$ are given by eq. 3.7, with $N_{\phi_{MW}}$ the number of occurrences for a given phase ϕ_{MW} and N_0 the total number of measurements. A statistical analysis, of the analytic expression eq. 3.7, will be carried out. Therefore the question was asked, what is number n of relative occurrences for a given phase ϕ_{MW} for N_0 measurements? Where the distribution of phases is uniform in the interval $[0, 2\pi]$. The probability of occurrences for a given phase is then given by

$$p(\phi, s, c) = s \cdot \left(\frac{1 + c \cos(\phi_{MW})}{2} \right) \quad (4.2)$$

When asking for the expectation value of relative occurrences it has to be accounted for the binominal nature of the measurement. The expected number of relative occurrences n is binominal distributed and given by the underlying binominal probability distribution.

$$B_{N_0, p}(n) = \binom{N_0}{k} p^n (1 - p)^n \quad (4.3)$$

The spread of the number of atoms per measurement N follows a poissonian distribution. The expected number of relative occurrences n per bin can then be calculated by the convolution of the two underlying probability functions.

$$\frac{N_n}{N_0} = \sum_{N-4\sigma_{N_0}}^{N+4\sigma_{N_0}} e^{-N_0} \cdot \frac{N_0^N}{N!} \cdot \int_0^{2\pi} d\phi B_{N_0, p, k}(\phi) \quad (4.4)$$

With the use of this analysis technique the Ramsey fringes are insensitive to a homogeneous decoherence source. A homogeneous decoherence source present in the apparatus, leads to a phase mismatch between the different measurements N_0 washing out the Ramsey fringe and reducing the contrast. Since the measurement is carried out in free fall, one can therefore classify the decoherence effect produced by magnetic field fluctuations between homogeneous or inhomogeneous decoherence.

Out of the obtained Ramsey fringe measurements the evolution of the contrast $c(\tau)$ for different Ramsey times can be estimated. For the analytic contrast analysis a coherence time $T_2 \approx 600 \mu s$ can be obtained, whereas in the case of the statistical contrast analysis no decay of the contrast is observable. As explained above, this is interpreted as a result of the fact, that the qubit is mostly subset to homogeneous shot-to-shot magnetic field noise. Homogeneous dephasing leads to a shift of the resonance and is visible

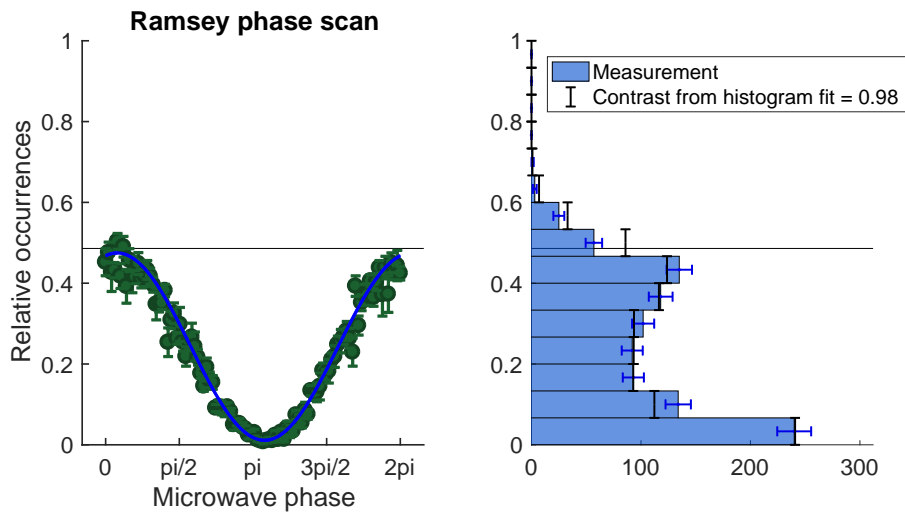


Figure 4.6: Exemplary results for a free fall ramey fringe measurement for a ramsey time of $1 \mu\text{sec}$. Where we see on the left an analytic contrast analysis and on the right a statistical contrast analysis. The horizontal line corresponds to the measured survival.

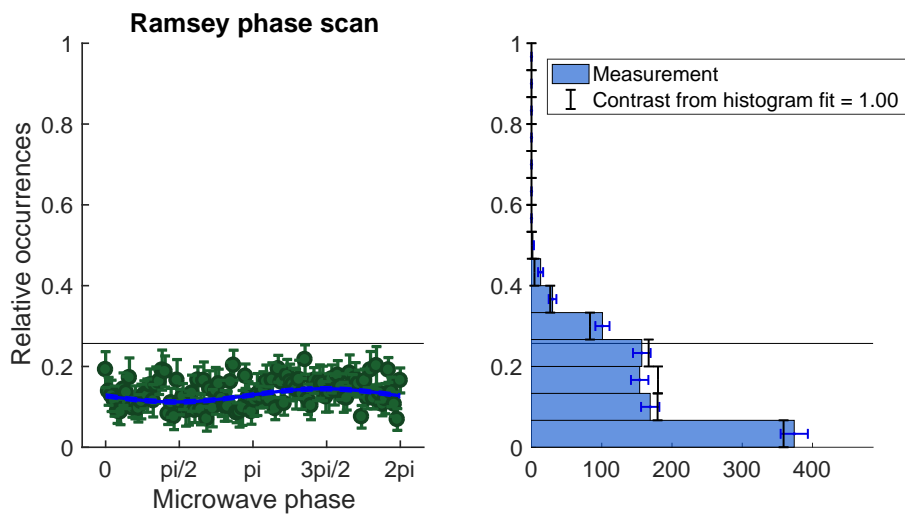


Figure 4.7: Exemplary results for a free fall ramey fringe measurement for a ramsey time of $1200 \mu\text{sec}$. Where we see on the left an analytic contrast analysis and on the right a statistical contrast analysis. The horizontal line corresponds to the measured survival.

as a phaseshift in the Ramsey fringe, leading to a loss of contrast in the analytic analysis, whereas this does not reduce the contrast in the statistical analysis.

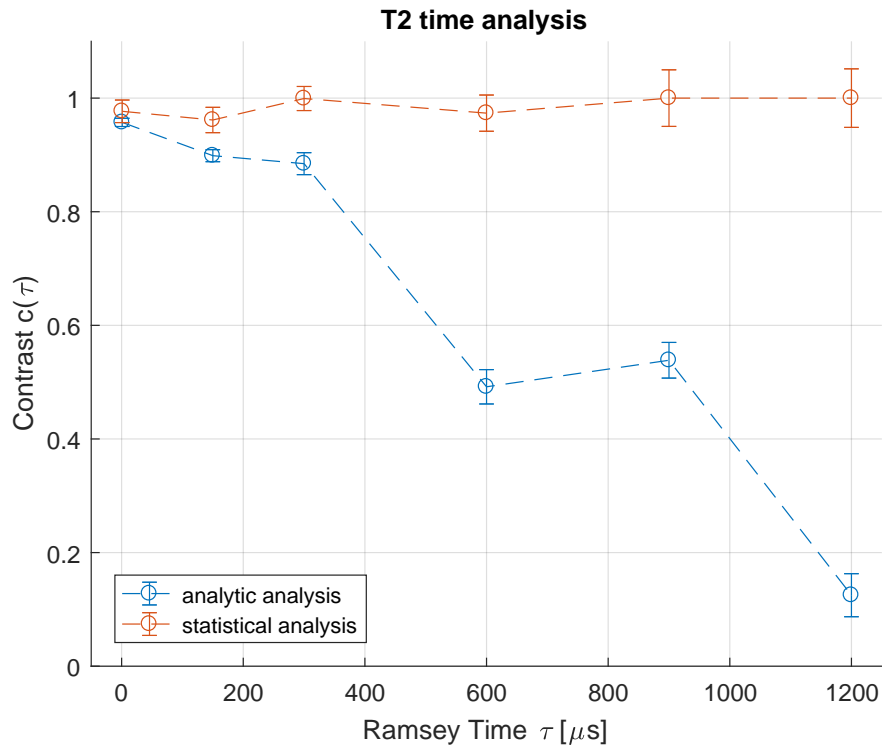


Figure 4.8: Evolution of the contrast $c(\tau)$ for different Ramsey times obtained out of a free fall Ramsey fringe in blue and out of a statistical analysis of the ramsey interferometry in orange.

Time analysis of magnetic field noise

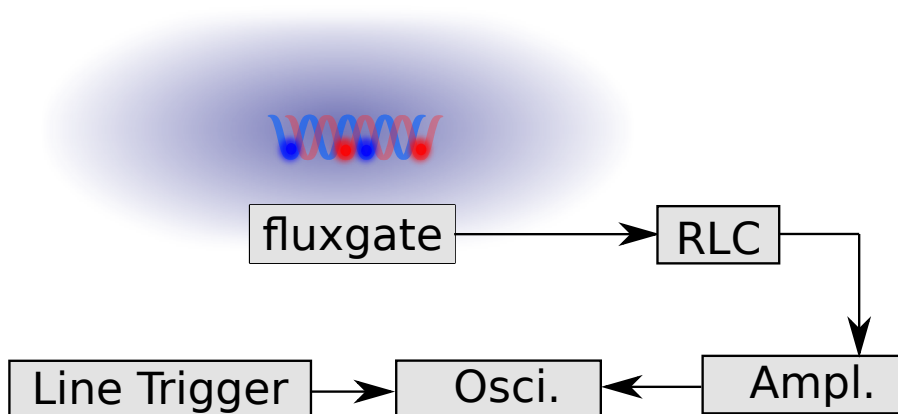


Figure 4.9: measurement setup of magnetic field noise measurement. The magnetic field parallel to the quantization axis of the implemented qubit is measured with the fluxgate sensor. A RLC filter with a cutoff frequency of 2 kHz is used to suppress sensor noise above 2 kHz. After the bandfilter a low noise high precision amplifier is used to get out of the read out noise of the oscilloscope, which is used for the data acquisition. Each measurement is synced to the line trigger, to achieve a time synchronization to the 50 Hz line ripple.

The aim is to measure the magnetic field noise, atoms experience during the ramsey time τ . Knowing, that the biggest contribution of magnetic field noise in our apparatus originates from 50 Hz noise, the

apparatus is triggered to the 50 Hz ripple in the power line. Timing the experiment with respect to the 50 Hz-ripple, makes the 50 Hz noise a repetitive contribution in all measurements. A schematic drawing of the measurement setup can be found in 4.9. It is assumed, that the obtained noise signal $S(t)$ consists out of two parts. One which is coherent in time and one which is noncoherent in time. Where $S(t)$ is the sum of the time coherent part $C(t)$ and the noncoherent part $n(t)$.

$$S(t) = C(t) + n(t) \quad (4.5)$$

The aim is to separate the coherent part from the noncoherent, observing N realisations during a chosen investigation time. Out of the observed noise $S_i(t)$ the average value over all realisations, will give access to both parts of the noise signal $S(t)$, Where the averaged value of the noise signal $S(t)$ for N realisations is given as

$$\langle S(t) \rangle_N = \frac{1}{N} \sum_{i=1}^N S_i(t) \quad (4.6)$$

Since $C(t)$ is coherent in time the averaged signal $\langle C(t) \rangle$ is equal to the non averaged signal $C(t)$.

$$\langle C(t) \rangle_N = C(t) \quad (4.7)$$

Whereas in the case of the noncoherent part of the signal, this does not hold true. The averaged noncoherent part $\langle n(t) \rangle_N$ of the signal will decay with the square root of the number of repetitions.

$$\langle n(t) \rangle \rightarrow \frac{1}{\sqrt{N}} \quad (4.8)$$

It is therefore possible to obtain the noncoherent part of the noise in the apparatus by subtracting the coherent $C(t)$ part from the initial noise $S(t)$.

$$C(t) = S(t) - \langle S(t) \rangle_N \quad (4.9)$$

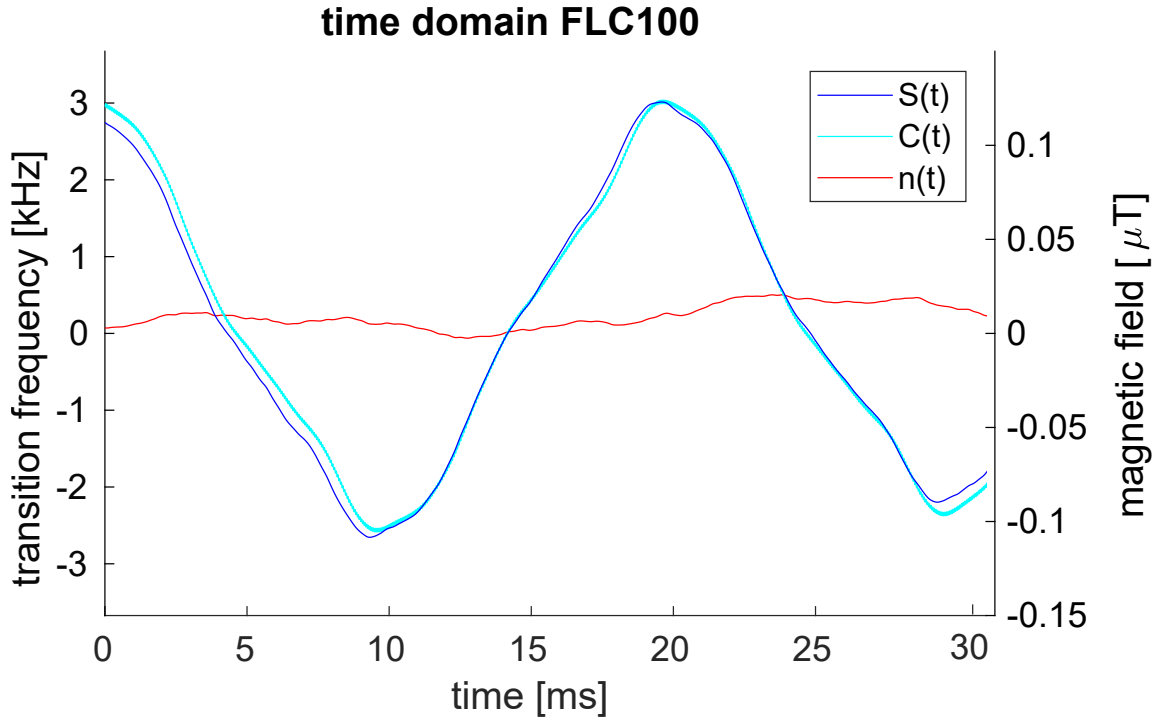


Figure 4.10: Temporal evolution of $B_{\text{fluxgate}}(t)$ measured with the fluxgate sensor. In blue the first repetition. In cyan coherent noise $C(t)$. In red the non coherent noise of the first repetition. One can see, that most of the noise is coherent in time. The measured magnetic field noise is also displayed in associated transition frequency change of the implemented qubit.

Statistical analysis of magnetic field noise

To achieve a deeper insight into the magnetic field noise present in the apparatus, a statistical analysis of the recorded field noise is carried out. It is interesting to test the stability of the experienced 50 Hz noise, and thereby test if a feed forward stabilisation of magnetic field noise is applicable on the 50 Hz noise due to its stability. Analysing the DC value and the linear drift of the magnetic field noise, can deliver a deeper insight about the shot-to-shot noise present in the apparatus. To get a good measure for these quantities a cosine fit of the following form, is carried out to each repetition:

$$B(t) = a_1 + a_2 \cdot t + a_3 \cos(2\pi b t + c_1) + a_4 \cos(6\pi \cdot b t + c_2) \quad (4.10)$$

Where the coefficients are given by a_1 the DC-offset, a_2 the linear drift, a_3 the amplitude of 50 Hz noise, a_4 the amplitude of the third higher harmonic of the 50 Hz noise, b the frequency of the 50 Hz noise, c_1 and c_2 the phase of the periodic noise contributions. In this way the main characteristics of the magnetic field noise can be caught out of the fit coefficients. The analysis is carried out in associated transition frequency change of the implemented qubit.

Analysis of the stability of 50 Hz noise

Taking a look at the fit coefficients a_3 (amplitude of 50 Hz noise) of all repetitions N , information on the amplitude of the 50 Hz noise can be obtained, see fig 4.11. The result reveals that the current 50 Hz magnetic field noise leads to an associated frequency shift of $\Delta f_B \approx 6.6$ kHz. Out of the spread of the distribution one can obtain a measure for the stability of the amplitude in time. The width of the distribution of amplitude coefficients is around 0.4 kHz, leading to a relative variation of the amplitude coefficients below 10%. Indicating a limit for a feed forward stabilisation on the order of 400 Hz.

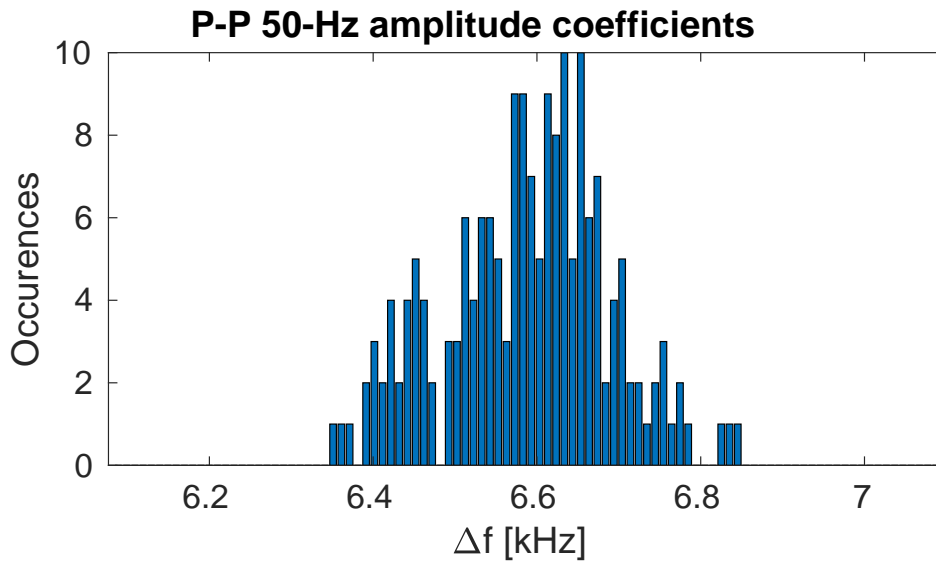
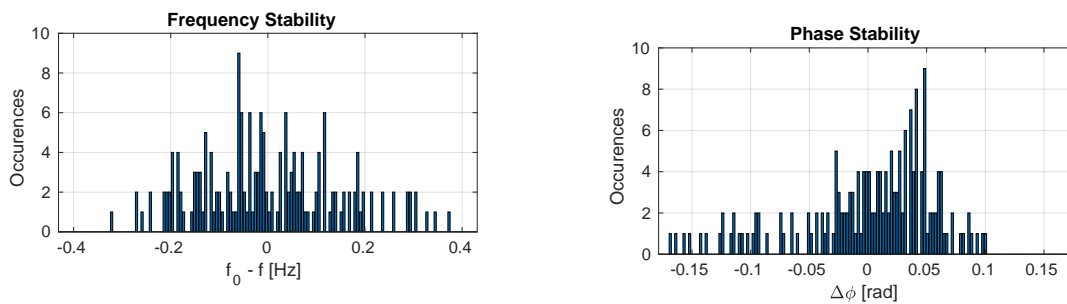


Figure 4.11: Distribution of 50 Hz noise amplitudes expressed in associated transition frequency change.

Out of the obtained fit coefficients b (frequency of 50 Hz noise) and c_1 (phase of 50 Hz noise) the frequency and phase of the fitted noise measurements can be extracted and its temporal stability can be estimated, see fig(4.12(a),4.12(b)). For the frequency distribution of the present 50 Hz noise a gaussian



(a) Distribution of the obtained frequency deviation for the fitted 50 Hz noise.

(b) Distribution of phases for the fitted 50 Hz noise signal

distribution is observed, up to a frequency deviation of ± 0.2 Hz which amounts to 0.6 %. Also the phase-jitter is smaller than 2.3 %.

These results deliver a promising result for a feed forward compensation for the 50 Hz magnetic field noise, indicating a possible suppression of associated transition frequency change of the qubit down to 400 Hz.

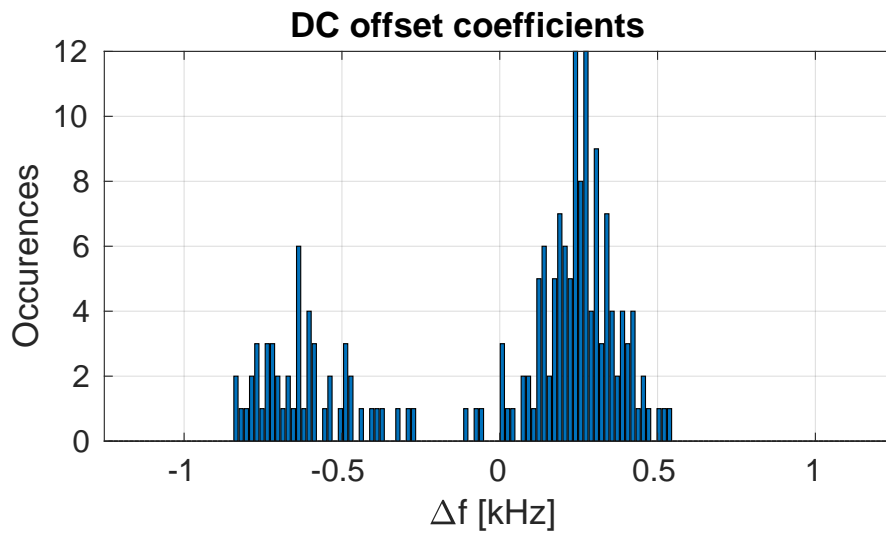


Figure 4.13: Distribution of fit coefficients a_1 indicating the DC-offset fluctuations obtained out of the magnetic field noise measurement.

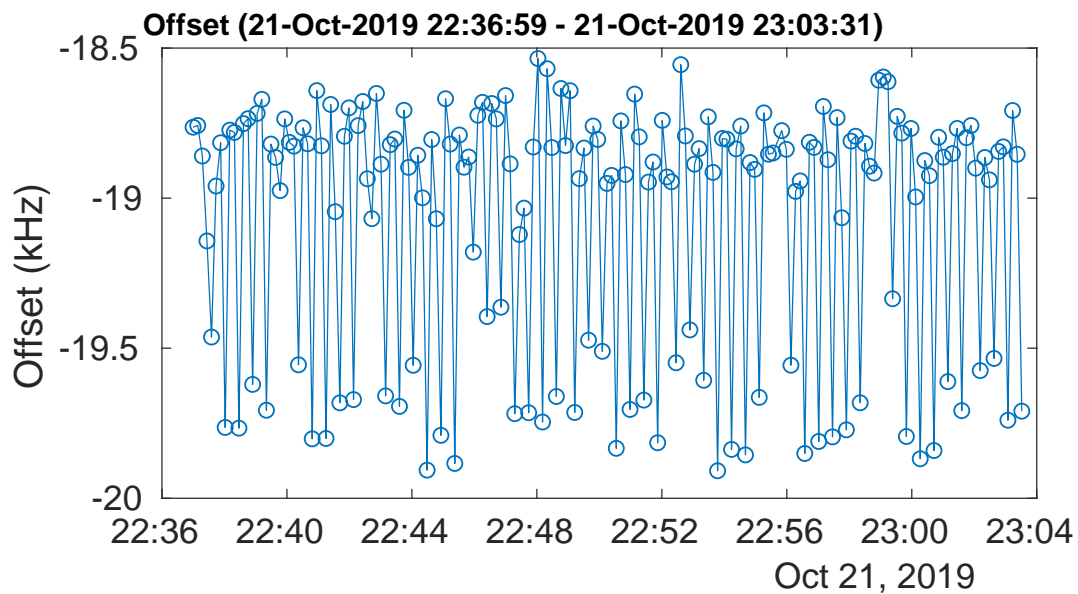


Figure 4.14: temporal evolution of fit coefficients a_1 indicating the DC offset obtained out of the magnetic field noise measurement.

Shot-to-shot noise analysis

Out of the fit coefficients a_1 (DC-offset) of all repetitions N , information on the shot-to-shot DC magnetic field variations can be obtained (fig 4.13). The resulting distribution reveals a total spread which leads to a shift of $\Delta f_B \approx 0.8$ kHz in transition frequency. The underlying distribution of the DC-offset coefficients shows a bimodal shape, with maxima at -0.5 kHz and 0.3 kHz associated transition frequency. Both maxima show an individual spread on the order of 0.4 kHz, with different peak heights. Taking a look at the temporal evolution of the DC-offset coefficients (fig. 4.14) a switching between the two modes of the DC offset is observable.

Taking a look at the distribution of the coefficients a_2 (linear drift) of all measurements N , information on the linear drift present in each measurement can be obtained (fig. 4.15). The distribution of linear drifts is centered around 0.03 kHz/ms and has a spread of 0.01 kHz/ms. Since the usual interrogation time of the apparatus is on the order of several μs this leads to a very small transition frequency shift below several Hz.

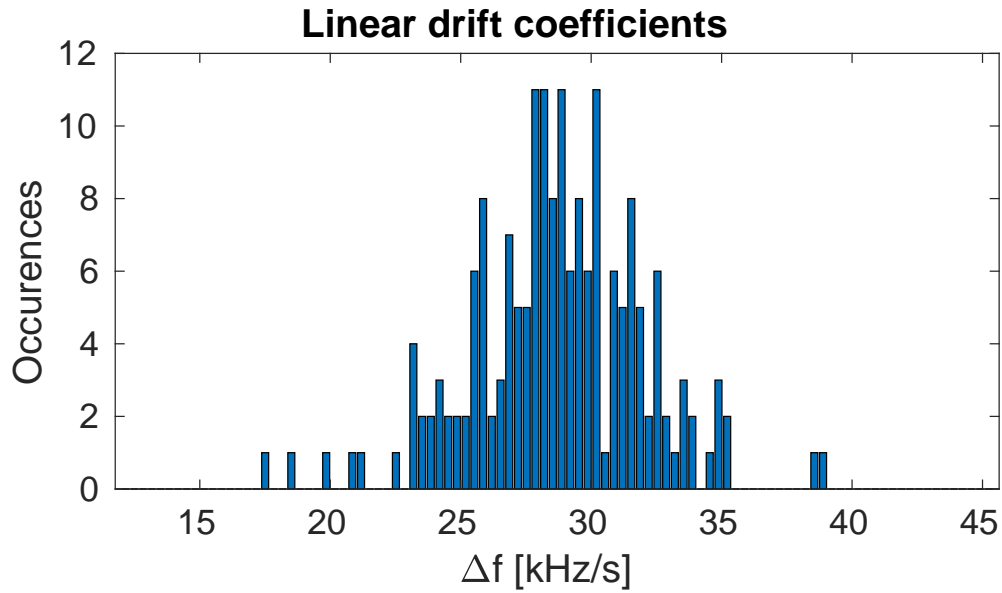


Figure 4.15: distribution of fit coefficients a_2 indicating the linear drift obtained out of the magnetic field noise measurement.

Frequency analysis of magnetic field noise

A frequency analysis of the underlying noncoherent magnetic field noise $n(t)$ has been carried. To do so, the spectral noise density of the underlying magnetic field noise has to be calculated. The spectral power density can be calculated out of the fourier transformation of the time-domain signal. To catch a maximum of information we want to compare two different approaches on how to calculate the spectral noise density. The first approach is to calculate the spectral noise density out of the average over all spectral power densities of the N_0 time-domain measurements. The spectral power density for a single time-domain measurement is then given by

$$S_{B,\text{single}}(\nu) = \frac{2\Delta t^2}{T} \left| \sum_{n=1}^{N/2+1} B_n(t) \exp^{-i\nu n\Delta t} \right|^2 \quad (4.11)$$

Where Δt is the sampling time, T the maximum period of a single time-domain measurement and N the number of points per time-domain measurement. The average over all spectral power densities is then given by

$$\bar{S}_{B,\text{average}} = \frac{1}{N_0} \sum_{n=0}^{N_0} S_{B,\text{fluxgate}} \quad (4.12)$$

The second approach is to calculate the spectral noise density out of the concatenated time-domain measurements. A better frequency resolution is achieved, for the lower frequency part. The spectral power density is then given by

$$S_{B,\text{concatenated}}(\nu) = \frac{2\Delta t^2}{T} \left| \sum_{n=1}^{(N \cdot N_0)/2+1} B_n(t) \exp^{-i\nu n\Delta t} \right|^2 \quad (4.13)$$

Where Δt is the sampling time, T the maximum period of all concatenated time-domain measurements. Due to the calculation of $S_{B,\text{concatenated}}$ two artefacts are present. First there is a strong spectral leakage at frequencies that are multiples of the smallest resolvable frequency of a single time-domain measurement. The origin of this artefact is a sudden jump of the magnetic field, at the time where the time-domain series are concatenated. Concluding that the spectral information is not physical, but the noise power of this spectral components is. This artefact is accounted for, by manually subtracting the power of this frequency components and shifting it to the lowest frequency components of $S_{B,\text{concatenated}}(\nu)$. The second artefact originates from the subtraction of the coherent part of the time-domain signal, creating a sharp drop of the noise power density to zero, with a frequency width of $\frac{1}{T_{\text{concatenated}}}$. It is accounted for this artefact, by carrying out a bandlimiting filter, with appropriate bandlimits for the corresponding frequency decades.

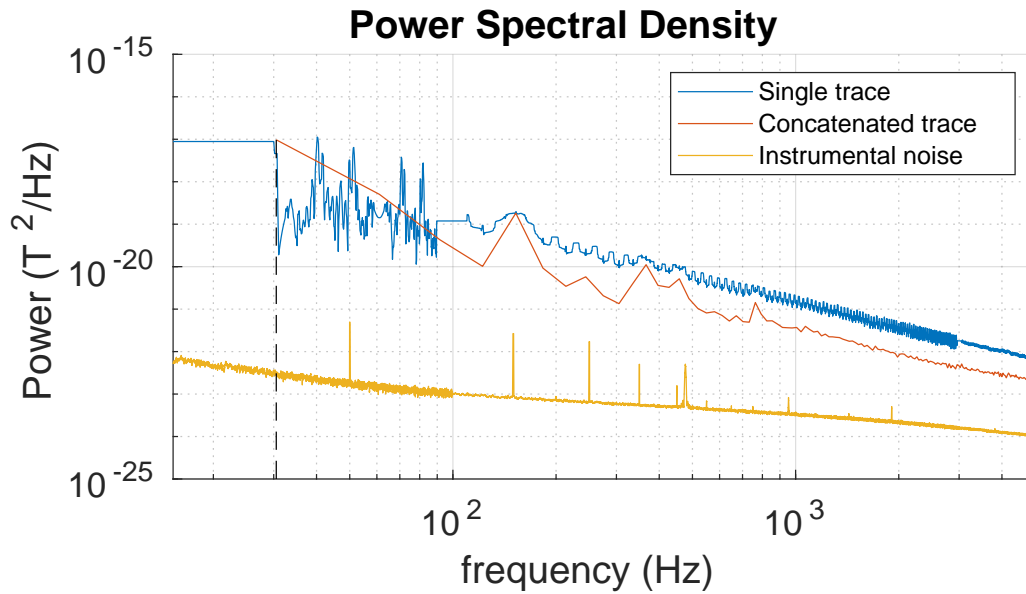


Figure 4.16: spectral noise power density of time-domain measurement of noncoherent magnetic field noise. In blue the obtained power density spectrum obtained of the concatenated time-domain measurement. In orange the power density spectrum obtained out of the averaged noise power densities. In yellow the instrumental noise of the measurement setup.

Looking at the obtained noise power spectral densities for the noncoherent magnetic field noise (fig 4.16) it is observable that the main contribution of noise lies in the spectral lowest resolvable frequency and is decreasing for higher frequencies. The absence of a peak at a frequency of 50 Hz indicates the high stability of the noise contribution due to the line ripple, as already discussed in sec.4.2.1. On top of that one can see that both analysis techniques, to calculate the spectral noise density agree. Also a higher resolution in the low frequency domain is observable. To give a more intuitive quantity the RMS value of the noncoherent magnetic field noise expressed in transition frequency change has been calculated revealing $\Delta f_{RMS} = 660$ Hz.

4.2.2 Estimate of decoherence due to magnetic field noise measurement

In the following an analysis technique of decoherence in our apparatus at the example of noncoherent magnetic field noise is presented.

The aim is to obtain an estimate of decoherence due to noncoherent magnetic field noise (section 4.2.1) present in the apparatus.

The decoherence in the apparatus will be estimated out of the spectral noise density as well as out of the spread of accumulated phases in time domain. An investigation of the underlying probability density function of accumulated phases will indicate the right measure to estimate the dephasing due to noncoherent magnetic field noise in the apparatus.

A correct estimated decoherence and measured decoherence out of a free fall Ramsey interferometer will be presented, showing a full understanding of the underlying mechanisms of decoherence due to magnetic field noise. Indicating the value of the applied analysis technique.

Statistical analysis of accumulated phases

When aiming to estimate the decoherence present in the apparatus, taking a look at the distribution of accumulated Ramsey phases for all repetitions i for a given Ramsey time τ , is necessary since it indicates the right measure to use, to estimate the decoherence. On top of that it can yield deeper insight in the dephasing mechanisms of our qubit and help understanding the origins of the loss of coherence. The accumulated phase of the qubit for a given Ramsey time τ due to noncoherent magnetic field noise can be calculated by integrating the associated transition frequency shift in time.

$$\Delta\phi_i = 2\pi \cdot \int_{\tau_0}^{\tau} f_i(\tau) d\tau = 2\pi \cdot \sum_{\tau_0}^{\tau} f_i(\tau) \Delta\tau \quad (4.14)$$

Where f is the noncoherent noise, expressed in associated transition frequency change of the implemented qubit.

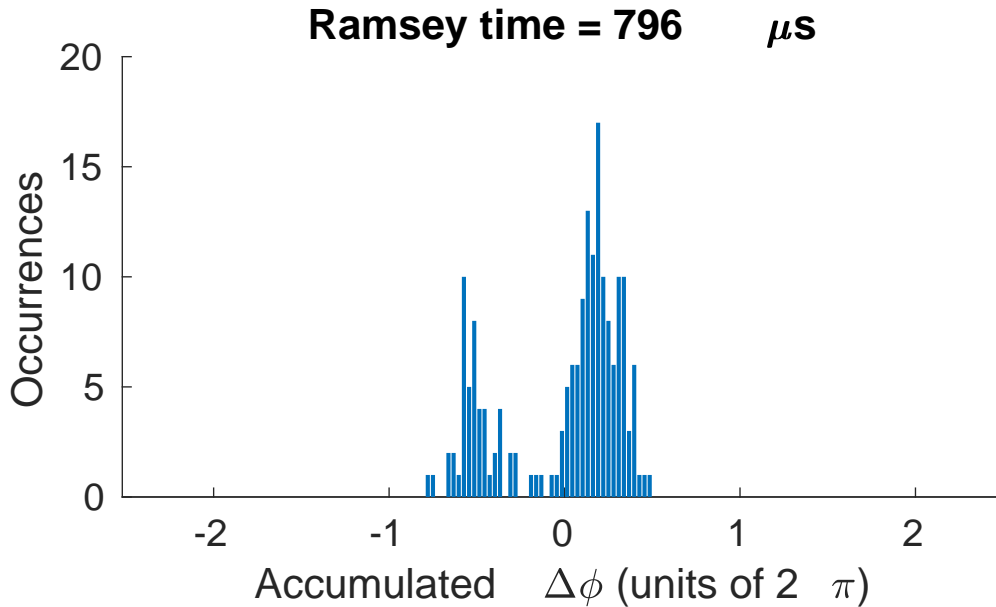


Figure 4.17: Distribution of accumulated phases $\Delta\phi$ for a Ramsey time $\tau = 796 \mu s$ obtained out of the measure of noncoherent magnetic field noise present in the apparatus.

A bimodal distribution of accumulated phases is observable, fig 4.17. Leading to a total spread of accumulated phases of 2π . Taking a look at each individual peak of the bimodal distribution reveals a spread smaller than π . The bimodal spread of phases, can be explained by DC magnetic field fluctuations between different repetitions i and j ($i \neq j$), see figure 4.13, leading to a phase mismatch between different measurements and can be interpreted as shot-to-shot noise in the apparatus. The bimodal shape of the spread of accumulated phases, has severe effects on the correct estimate of the decoherence using different measures, as will be discussed in sections 4.2.2.

Loss of contrast $c(t)$ due to magnetic field noise spectral power density

Using the obtained spectral power densities (fig 4.16) as a measure, an estimate for the expected decoherence of the qubit can be obtained. The loss of contrast due to magnetic field noise is given after [15] as

$$c(\tau) = \exp(-\Delta\Phi^2/2) \quad (4.15)$$

where

$$\Delta\Phi^2(\tau) = \frac{\mu_B^2}{\hbar^2} \cdot [g_F(\uparrow)m_F(\uparrow) - g_F(\downarrow)m_F(\downarrow)]^2 \cdot \tau^2 \sum_{\nu=\nu_0}^{\nu_{\max}} \text{sinc}(\pi\nu\tau)^2 \cdot S_B(\nu) \quad (4.16)$$

Where $-g_F(\uparrow) = g_F(\downarrow) = -1/4$ the landé factor for the given Cs¹³³ states [23] and $m_F(\uparrow) = 3$ and $m_F(\downarrow) = 4$ for the utilised qubit system.

Using the noise power density to obtain a measure of the decoherence a real noncoherent magnetic field noise is implied. The integral over the spectral power density is given by the variance of the underlying variable, for a mean zero signal.

$$\int d\nu S_B(\nu) = \sigma_B^2 \quad (4.17)$$

Using the power density spectrum to obtain a measure of decoherence in the apparatus, the information of the noise is reduced to the spread of the underlying distribution, which is given by the σ_B . In case of a gaussian distributed noise, the loss of contrast can be obtained out of the power density of the associated phases since there is no loss of information. A gaussian distribution is well described by its variance σ^2 . Therefore equation 4.16 is applicable and delivers a precise estimate of the decoherence due to magnetic field noise. Taking a look at the result of the estimate of decoherence out of the spectral power density of

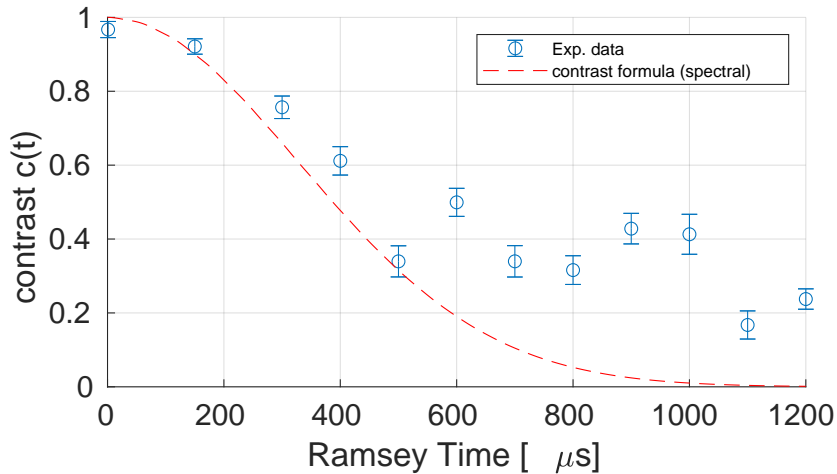


Figure 4.18: Decay of contrast due to a Ramsey free fall measurement in red together with a estimate of the decay of contrast measured out of the power density spectrum of magnetic field noise.

the magnetic field noise, compared to the actual decay of contrast out of a free fall Ramsey interferometer, figure 4.18. One can see, that the overall trend of the decay of contrast is reproducible by the estimate of

the decay of contrast. Whereas a revival is observable in the contrast obtained out of a free fall Ramsey fringe. This characteristic of the evolution of the contrast is not present in the estimate due to magnetic field noise. As explained in section 4.2.2 the revival of contrast is explainable by the bimodal spread in the distribution of accumulated phases, this information is not taken into account by eq. 4.16. Taking this information into account one can find a measure of the decay of contrast due to the magnetic field noise showing the same behaviour as the obtained decay of contrast by a free fall Ramsey interferometer.

Loss of contrast measured from time domain

Out of the time domain measurements of magnetic field fluctuations an estimate of the decoherence can be found. The decay of contrast $c(\tau)$ of a Ramsey interferometer can be calculated by averaging all obtained phases, for a given Ramsey time τ [35].

$$c(\tau) = |\langle e^{-i\phi(\tau)} \rangle| \quad (4.18)$$

Where the phase is given by the associated frequency shift of the qubit due to the measured noncoherent magnetic field noise.

The estimate of the decay of contrast obtained out of eq. 4.18 can reproduce the behaviour of the

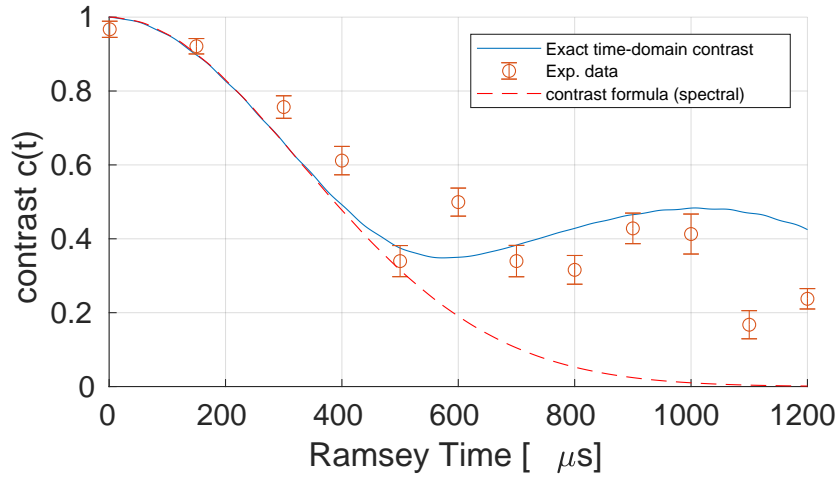


Figure 4.19: Contrast measured in free fall (orange) together with the contrast estimated out of the power density spectrum of magnetic field noise (blue) and an estimate out of the magnetic field noise measurement in time domain (dashed red).

experimentally measured contrast. In contrast to the estimate out of the spectral contrast formular, also the revival of the contrast can be recaptured. The effect of a bimodal distribution of phases can be discussed by splitting up the distribution of phases. Assuming the bimodal distribution originating from a constant phase offset, in this particular case the distribution of phases can be treated as two equal distributions separated by a constant phase ϕ_c .

$$|\langle e^{-i\phi(\tau)} \rangle| = |\langle e^{-i\phi_1} \cdot e^{-i\phi_2} \rangle| \quad (4.19)$$

$$= |\langle e^{-i\phi_1} \rangle + \langle e^{-i\phi_1} \rangle \cdot e^{-i\phi_c}| \quad (4.20)$$

which can be rewritten as

$$|1 + e^{-i\phi_c}| |\langle e^{-i\phi} \rangle| \quad (4.21)$$

For $\phi_2 = \pi$ a drop of the contrast to zero, can be found due to the bimodal nature of the spread of phases. As from sec. it is known 4.2.1 that DC magnetic field fluctuations are present on the order of an associated frequency shift of $f_B \approx 800$ Hz. The time when the contrast drops to zero, can be estimated by

$$\tau = \pi/f_B \quad (4.22)$$

$$\tau \approx 625\mu s \quad (4.23)$$

Which agrees nicely with the drop of the contrast in the obtained estimate of the decoherence due the measured magnetic field noise. The nonzero dropping of the estimated contrast is due to the different heights of the distribution of DC magnetic field fluctuations.

Magnetic field post correction

In the following it will be reported about a magnetic field post correction. The aim is to use the recorded magnetic field noise to correct for the qubit transition frequency shift due to magnetic field fluctuations. First a calibration of the magnetic field at the sensors position to the position of the atoms has been carried out. Afterwards a post correction on the example of a free fall Ramsey interferometer is presented.

Sensor-atom calibration

To reduce the deviation of the magnetic field fluctuations at the position of the sensor to the position of the atoms, a calibration has been carried out. Two fluxgate magnetometers are used placed equally far away from the position of the atoms, aligned with the magnetic quantization field. By recording a microwave spectrum in free fall the transition frequency of the atoms is extracted, while at the same time the magnetic field is recorded. To extract the temporal evolution of the qubit transition frequency due to the magnetic field fluctuations the measurement is repeated multiple times.

Finally, a weighted average of the two sensors plus an offset is computed and subtracted from the fitted qubit transition frequency to corrected the measured qubit transition frequency.

$$f_{\text{corrected}} = f_{MW} - (s_1 f_{S1} - s_2 f_{S2} + f_0) \quad (4.24)$$

Where $f_{\text{corrected}}$ is the corrected qubit transition frequency, f_{MW} is the qubit transition frequency shift extracted out of the microwave spectrum, f_{S1} and f_{S2} the recorded magnetic field noise expressed in associated qubit transition frequency, s_1 and s_2 are the weights for the two sensors and f_0 a constant offset.

The calibration is then carried out by finding the optimal parameter set s_1, s_2 and f_0 , by minimizing the RMS of $f_{\text{corrected}}$, see fig 4.20. By the use of the optimal scaling parameter set, the resilient fluctuation of the corrected qubit transition frequency in time can be minimized to

$$RMS(f_{\text{corrected}}) = 0.0571 \text{ kHz.} \quad (4.25)$$

.

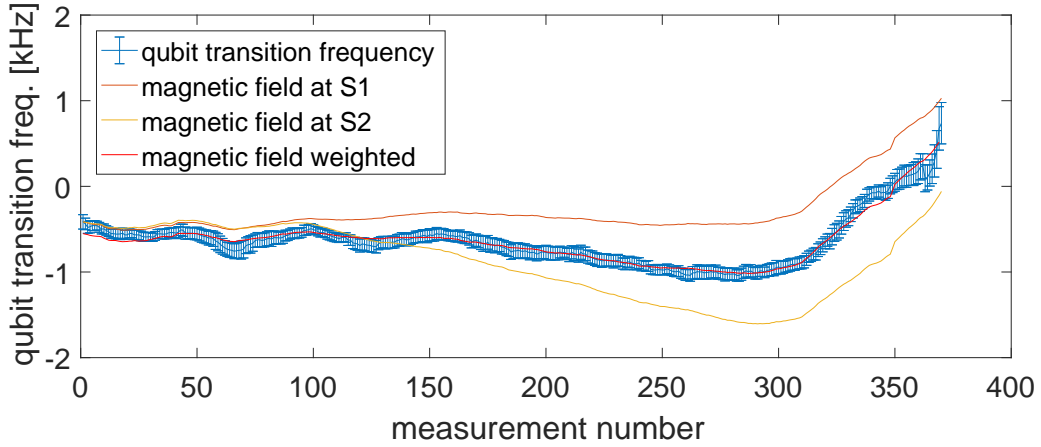


Figure 4.20: Temporal evolution of the qubit transition frequency in blue, magnetic field at sensor position 1 in orange, magnetic field at sensor position 2 in yellow and the predicted magnetic field at the position of the atoms in red. The magnetic field is display in qubit transition frequency.

Correction of Ramsey fringe

Using the measured magnetic field of the calibrated fluxgate magnetometers a Ramsey fringe can be post corrected. To do so, the magnetic field during the Ramsey time for each point of the Ramsey fringe is recorded. Out of the magnetic field, the accumulated phase is computed (eq. 4.14), to correct the according Ramsey phase of each point. This way the Ramsey fringe is post corrected, see fig 4.21. In sec. 4.2.2 it was shown, that for a Ramsey time of $\tau \approx 625\mu\text{s}$, the largest drop of contrast due to a bimodal spread of the accumulated phases is expected. A clear improvement of the contrast extracted out of the

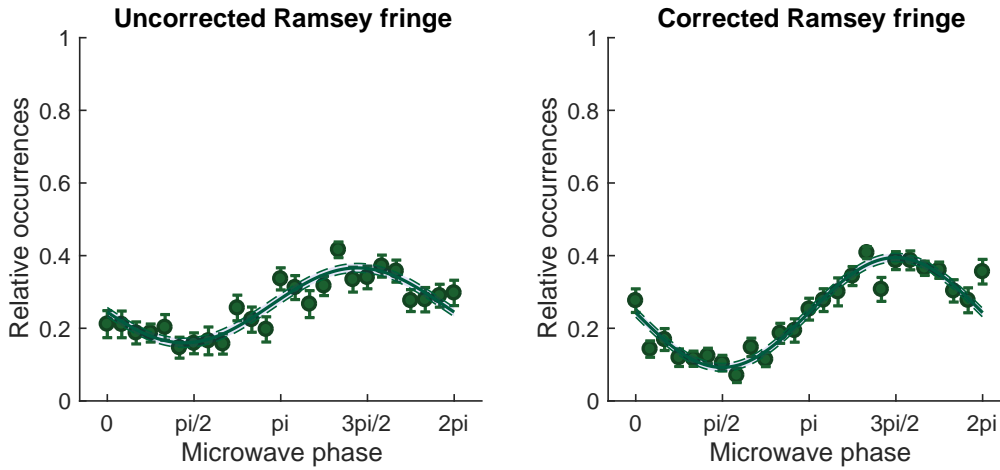


Figure 4.21: (left) Recorded Ramsey fringe in free fall for a Ramsey time $\tau = 600\mu\text{s}$. (right) Ramsey fringe in free fall with magnetic field post correction.

Ramsey fringe (fig. 4.21) is visible. The corrected as well as the uncorrected contrast, obtained out of the Ramsey fringe are given by

$$c_{\text{uncorrected}} = 0.366 \pm 0.023 \quad (4.26)$$

$$c_{\text{corrected}} = 0.804 \pm 0.017 \quad (4.27)$$

Performing a post correction improves the contrast of about 220 % can be reported.

The evolution of the contrast for different Ramsey times reveals an overall improvement of the contrast, in the case of an applied post correction. It can be reported of a coherence time of $T_{2,\text{corrected}} \approx 1\text{ms}$, whereas in the uncorrected case a coherence time of $T_{2,\text{uncorrected}} \approx 600\ \mu\text{s}$ yielding a nice improvement of the coherence time. Since the measurements have been performed in free fall the resilient decay of contrast is due to homogeneous magnetic field fluctuations which cannot be post compensated, indicating a limit of the post correction. A potential improvement of the post correction could be achieved by using independent sets of scaling parameters, as it was not the case here, where a global set of scaling parameters has been used for all Ramsey fringes.

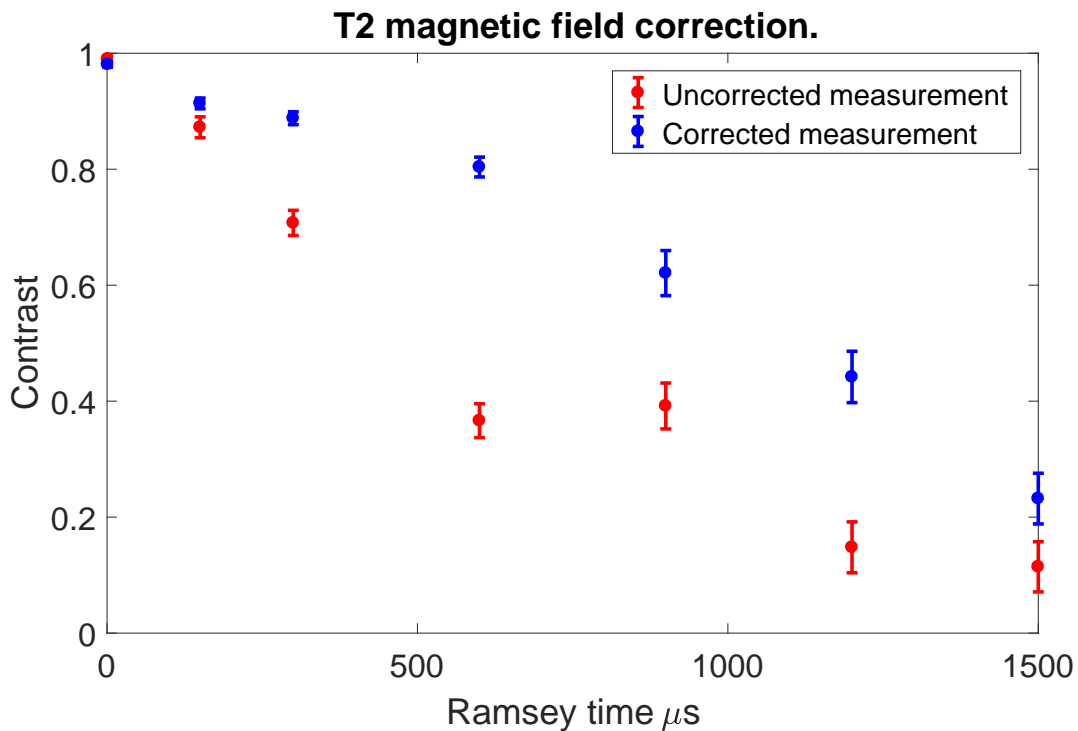


Figure 4.22: Evolution of contrast for different Ramsey times, obtained out of free fall Ramsey interferometry. In blue a magnetic field post correction has been performed. In red the uncorrected contrast evolution.

Conclusion and outlook

When I started my master thesis at the state dependent optical lattice experiment in Bonn, the coherence time was measured to be around $\approx 75 \mu\text{s}$, for cesium atoms stored in an optical lattice.

While the physical effects leading to a decoherence of the qubit in the optical lattice were known, the dominating effect was unknown.

Investigating the effects leading to a decoherence of the apparatus was part of this masterthesis. The research began with the setup and implementation of a current stabilisation for the magnetic field driving current. It was possible to achieve a relative current stability of 10^{-6} , and therefore stabilise the magnetic field fluctuations produced by the driving current below an associated fluctuation of the qubit transition frequency of 100 Hz.

To suppress fluctuations of the qubit transition frequency due to external magnetic field fluctuations, a feed forward magnetic field stabilisation was set up and implemented, aiming at the cancellation of 50 Hz noise. Eventhough it was possible to stabilise on an electronic limit for the 50 Hz noise, which would have lead to an associated fluctuation of the qubit transition frequency below 500 Hz, it was not possible to transport the achieved stability onto the qubit transition frequency.

To solve this problem an in depth magnetic field analysis was invented and carried out, tailored to predict the atomic decoherence due to magnetic field fluctuations. Revealing DC magnetic field fluctuations, explaining the unreached electronic limit of the feed forward magnetic field stabilisation.

To test the prediction of the decoherence out of the magnetic field analysis, a measure of the decoherence due to magnetic field fluctuations has been carried out. Free fall Ramsey interferometry was used to obtain a measure of the coherence time out of the contrast of Ramsey fringes, revealing a coherence time of $T_2 \approx 500 \mu\text{s}$. To further classify the decoherence mechanism between homogeneous and inhomogeneous dephasing a statistical analysis, insensitive to homogeneous dephasing, of the free fall Ramsey fringes has been carried out. It was shown that the dephasing mechanism, on the considered time scales, is dominated by homogeneous dephasing and therefore has to be accounted to global magnetic field fluctuations rather than spatial gradient magnetic field fluctuations.

Coming back to the affore mentioned magnetic field fluctuation analysis technique, I was able to reproduce the decay of contrast and identify the main effect leading to a decoherence of the qubit. DC magnetic field offset fluctuations, on the order of 800 Hz associated qubit transition frequency change, causing a bimodal spread in the distribution of accumulated Ramsey phase, limiting the coherence time.

By the use of a software-wise post correction, I was able to show an improvement of coherence leading to a coherence time of $T_2 \approx 1 \text{ms}$. Indicating a limit for a future DC-magnetic field offset stabilisation. To achieve an even better coherence time an active stabilisation can be considered.

The results of my research also help to improve the affore mentioned (sec. 2.3.2) measurement of

the stress induced birefringence, for which a precise determination of the qubit transition frequency is necessary and can be achieved via a post correction of the measured transition frequency. To continue the investigation of decoherence effects the invented analysis technique should be used to measure the decoherence of the qubit due to intensity fluctuations of the lattice. The work presented in this thesis, can be classified as a contribution for the overall goal of a quantum cellular automata. Understanding and solving decoherence effects in the field of quantum information processing, is one of the main tasks on realizing a quantum cellular automata.

Bibliography

- [1] H. Frowein, *Titan-Saphir Laser Grundlagen und Anwendungen des wichtigsten Kurzpulslasersystems*, *Optik & Photonik* (2011) (cit. on p. 1).
- [2] C. E. Wieman and L. Hollberg, *Using diode lasers for atomic physics*, *Review of Scientific Instruments* **62** (1991) 1, eprint: <https://doi.org/10.1063/1.1142305>, URL: <https://doi.org/10.1063/1.1142305> (cit. on p. 1).
- [3] T. Brabec et al., *Kerr lens mode locking*, *Opt. Lett.* **17** (1992) 1292, URL: <http://ol.osa.org/abstract.cfm?URI=ol-17-18-1292> (cit. on p. 1).
- [4] H. J. Metcalf and P. van der Straten, “Laser Cooling and Trapping of Neutral Atoms”, *The Optics Encyclopedia*, American Cancer Society, 2007, ISBN: 9783527600441, eprint: <https://onlinelibrary.wiley.com/doi/pdf/10.1002/9783527600441.oe005>, URL: <https://onlinelibrary.wiley.com/doi/abs/10.1002/9783527600441.oe005> (cit. on p. 1).
- [5] W. Ketterle and N. V. Druten, *Evaporative Cooling of Trapped Atoms*, *Advances In Atomic, Molecular, and Optical Physics* **37** (1996) 181, ed. by B. Bederson and H. Walther, ISSN: 1049-250X, URL: <http://www.sciencedirect.com/science/article/pii/S1049250X08601019> (cit. on p. 1).
- [6] K. B. Davis et al., *Bose-Einstein Condensation in a Gas of Sodium Atoms*, *Phys. Rev. Lett.* **75** (22 1995) 3969, URL: <https://link.aps.org/doi/10.1103/PhysRevLett.75.3969> (cit. on p. 1).
- [7] T. P. Heavner et al., *First accuracy evaluation of NIST-F2*, *Metrologia* **51** (2014) 174, URL: <https://doi.org/10.1088%2F0026-1394%2F51%2F3%2F174> (cit. on p. 1).
- [8] N. Huntemann et al., *Single-Ion Atomic Clock with 3×10^{-18} Systematic Uncertainty*, *Phys. Rev. Lett.* **116** (6 2016) 063001, URL: <https://link.aps.org/doi/10.1103/PhysRevLett.116.063001> (cit. on p. 1).
- [9] D. A. Meyer, *From quantum cellular automata to quantum lattice gases*, *Journal of Statistical Physics* **85** (1996) 551, ISSN: 1572-9613, URL: <https://doi.org/10.1007/BF02199356> (cit. on p. 1).
- [10] C. Robens et al., *Low-Entropy States of Neutral Atoms in Polarization-Synthesized Optical Lattices*, *Phys. Rev. Lett.* **118** (6 2017) 065302, URL: <https://link.aps.org/doi/10.1103/PhysRevLett.118.065302> (cit. on p. 1).

- [11] M. Karski et al., *Quantum Walk in Position Space with Single Optically Trapped Atoms*, *Science* **325** (2009) 174, ISSN: 0036-8075, eprint: <https://science.sciencemag.org/content/325/5937/174.full.pdf>, URL: <https://science.sciencemag.org/content/325/5937/174> (cit. on p. 1).
- [12] C. Robens et al., *Ideal Negative Measurements in Quantum Walks Disprove Theories Based on Classical Trajectories*, *Phys. Rev. X* **5** (1 2015) 011003, URL: <https://link.aps.org/doi/10.1103/PhysRevX.5.011003> (cit. on p. 1).
- [13] C. Robens, *Testing the Quantumness of Atom Trajectories*, PhD thesis: University of Bonn, 2017 (cit. on pp. 1, 6, 7, 9, 13, 14).
- [14] T. Groh et al., *Robustness of topologically protected edge states in quantum walk experiments with neutral atoms*, *Phys. Rev. A* **94** (1 2016) 013620, URL: <https://link.aps.org/doi/10.1103/PhysRevA.94.013620> (cit. on p. 1).
- [15] A. Alberti et al., *Decoherence Models for Discrete-Time Quantum Walks and their Application to Neutral Atom Experiments*, *New J. Phys.* **16** (2014) 123052 (cit. on pp. 2, 9, 11, 35).
- [16] I. Bloch, *Ultracold quantum gases in optical lattices*, *Nature Physics* **1** (2005) (cit. on p. 3).
- [17] R. Grimm, M. Weidemüller and Y. B. Ovchinnikov, *Optical dipole traps for neutral atoms*, *Advances in Atomic, Molecular and Optical Physics* **42** (2000) (cit. on pp. 3, 6, 9).
- [18] S. Chu et al., *Experimental Observation of Optically Trapped Atoms*, *Phys. Rev. Lett.* **57** (3 1986) 314, URL: <https://link.aps.org/doi/10.1103/PhysRevLett.57.314> (cit. on p. 3).
- [19] J. D. Jackson, *classical electrodynamics*, vol. 3, John Wiley & Sons, 1999, ISBN: 0-471-30932-X (cit. on p. 4).
- [20] I. H. Deutsch and P. S. Jessen, *Quantum-state control in optical lattices*, *Phys. Rev. A* **57** (3 1998) 1972, URL: <https://link.aps.org/doi/10.1103/PhysRevA.57.1972> (cit. on p. 6).
- [21] D. Jaksch et al., *Entanglement of Atoms via Cold Controlled Collisions*, *Phys. Rev. Lett.* **82** (9 1999) 1975, URL: <https://link.aps.org/doi/10.1103/PhysRevLett.82.1975> (cit. on p. 6).
- [22] D. Döring, *Ein Experiment zum zustandsabhängigen Transport einzelner Atome*, 2007 (cit. on p. 6).
- [23] D. A. Steck, *Cesium D line data*, tech. rep., Theoretical Division (cit. on pp. 7, 35).
- [24] A. Steffen, *Single atom interferometers and Bloch oscillations in quantum walks*, PhD thesis: University of Bonn, 2013 (cit. on pp. 7, 10, 16).
- [25] J. Söding et al., *Giant Spin Relaxation of an Ultracold Cesium Gas*, *Phys. Rev. Lett.* **80** (9 1998) 1869, URL: <https://link.aps.org/doi/10.1103/PhysRevLett.80.1869> (cit. on p. 9).
- [26] J. D. Miller, R. A. Cline and D. J. Heinzen, *Far-off-resonance optical trapping of atoms*, *Phys. Rev. A* **47** (6 1993) R4567, URL: <https://link.aps.org/doi/10.1103/PhysRevA.47.R4567> (cit. on p. 9).

-
- [27] R. A. Cline et al., *Spin relaxation of optically trapped atoms by light scattering*, *Opt. Lett.* **19** (1994) 207, URL: <http://ol.osa.org/abstract.cfm?URI=ol-19-3-207> (cit. on p. 9).
- [28] S. B.P. Straughan, *Spectroscopy*, Chapman and Hall Ltd., 1976 (cit. on p. 9).
- [29] S. Kuhr et al., *Analysis of dephasing mechanisms in a standing-wave dipole trap*, *Phys. Rev. A* **72** (2 2005) 023406, URL: <https://link.aps.org/doi/10.1103/PhysRevA.72.023406> (cit. on pp. 10, 14).
- [30] C. G. Townsend et al., *Phase-space density in the magneto-optical trap*, *Phys. Rev. A* **52** (2 1995) 1423, URL: <https://link.aps.org/doi/10.1103/PhysRevA.52.1423> (cit. on p. 13).
- [31] A. M. Steane, M. Chowdhury and C. J. Foot, *Radiation force in the magneto-optical trap*, *J. Opt. Soc. Am. B* **9** (1992) 2142, URL: <http://josab.osa.org/abstract.cfm?URI=josab-9-12-2142> (cit. on p. 13).
- [32] P. D. Lett et al., *Optical molasses*, *J. Opt. Soc. Am. B* **6** (1989) 2084, URL: <http://josab.osa.org/abstract.cfm?URI=josab-6-11-2084> (cit. on p. 13).
- [33] S. Chu et al., *Three-dimensional viscous confinement and cooling of atoms by resonance radiation pressure*, *Phys. Rev. Lett.* **55** (1 1985) 48, URL: <https://link.aps.org/doi/10.1103/PhysRevLett.55.48> (cit. on p. 13).
- [34] C. Salomon et al., *Laser Cooling of Cesium Atoms Below 3 K*, *Europhysics Letters (EPL)* **12** (1990) 683, URL: <https://doi.org/10.1209%2F0295-5075%2F12%2F8%2F003> (cit. on p. 13).
- [35] S. C. Rand, *Lectures on Light: Nonlinear and Quantum Optics using the Density Matrix*, Oxford University Press, 2016 (cit. on pp. 14, 36).
- [36] M. Karski, *State-selective transport of single neutral atoms*, PhD thesis: University of Bonn, 2010 (cit. on p. 15).
- [37] W. HAPPER, *Optical Pumping*, *Rev. Mod. Phys.* **44** (2 1972) 169, URL: <https://link.aps.org/doi/10.1103/RevModPhys.44.169> (cit. on p. 16).
- [38] M. L. Citron et al., *Experimental study of power broadening in a two-level atom*, *Phys. Rev. A* **16** (4 1977) 1507, URL: <https://link.aps.org/doi/10.1103/PhysRevA.16.1507> (cit. on p. 16).
- [39] N. F. Ramsey, *A Molecular Beam Resonance Method with Separated Oscillating Fields*, *Phys. Rev.* **78** (6 1950) 695, URL: <https://link.aps.org/doi/10.1103/PhysRev.78.695> (cit. on p. 17).
- [40] L. Viola and S. Lloyd, *Dynamical suppression of decoherence in two-state quantum systems*, *Phys. Rev. A* **58** (4 1998) 2733, URL: <https://link.aps.org/doi/10.1103/PhysRevA.58.2733> (cit. on p. 23).
- [41] W. Yang, Z.-Y. Wang and R.-B. Liu, *Preserving qubit coherence by dynamical decoupling*, *Frontiers of Physics in China* **6** (2011) 2, ISSN: 2095-0470, URL: <https://doi.org/10.1007/s11467-010-0113-8> (cit. on p. 23).

- [42] B. S. Deaver and W. S. Goree, *Some Techniques for Sensitive Magnetic Measurements Using Superconducting Circuits and Magnetic Shields*, *Review of Scientific Instruments* **38** (1967) 311, eprint: <https://doi.org/10.1063/1.1720694>, URL: <https://doi.org/10.1063/1.1720694> (cit. on p. 47).

Useful information

A.1 Characterisation of fluxgate magnetometer

In the following it will be reported about the measurement of the instrumental noise of the used measurement setup.

A measurement of the instrumental noise of the measurement setup. The measurement setup is consisting out of a magnetic fluxgate magnetometer¹ followed by an RLC-filter with a cutoff frequency of 2 kHz, which is then amplified by a low noise amplifier². To measure the instrumental noise it would in principle require to shield the magnetometer from external magnetic field. This is in principle possible by using a mu-metal shieldings[42]. In the absence of a mu-metal shielding a different measurement technique has been realised.

The principle idea is to oppose two fluxgate magnetometer to measure the same signal. Out of the difference of the two signals a measure for an upper bound of the instrumental noise can be obtained. Assuming the signal measured with a magnetic fluxgate is given by

$$S_i = y + n_i \quad (\text{A.1})$$

Where S_i the measured signal is assumed to consist out of two contributions : y the actual magnetic field measured and n_i the instrumental noise. By minimizing the variance of the difference of the two sensors a introduced scaling factor α can be found, which accounts for a potential different sensitivity or a different signal amplitude y .

$$\min(\text{var}(S_1 - \alpha S_2)) \quad (\text{A.2})$$

Now an upper estimate for the instrumental noise of the magnetic field sensor can be found by taking the difference of the two measured signals.

$$n = 1/2 \cdot (S_1 - \alpha S_2) \quad (\text{A.3})$$

Out of the difference of the two signals, the spectra power density is calculated using the Wiener-Chintschin-Theorem. It can be reported on a SNR of up to 20 dB for frequencys below 1 kHz, see fig. A.2. For frequencies above 1 kHz, the signal gets burried by the experimental noise of the fluxgate sensor. This behaviour is due to the bandlimit of the fluxgate magnetometer of 1 kHz.

¹ Miniature Magnetic Field Sensor FLC 100

² SR560 — Low-noise voltage preamplifier

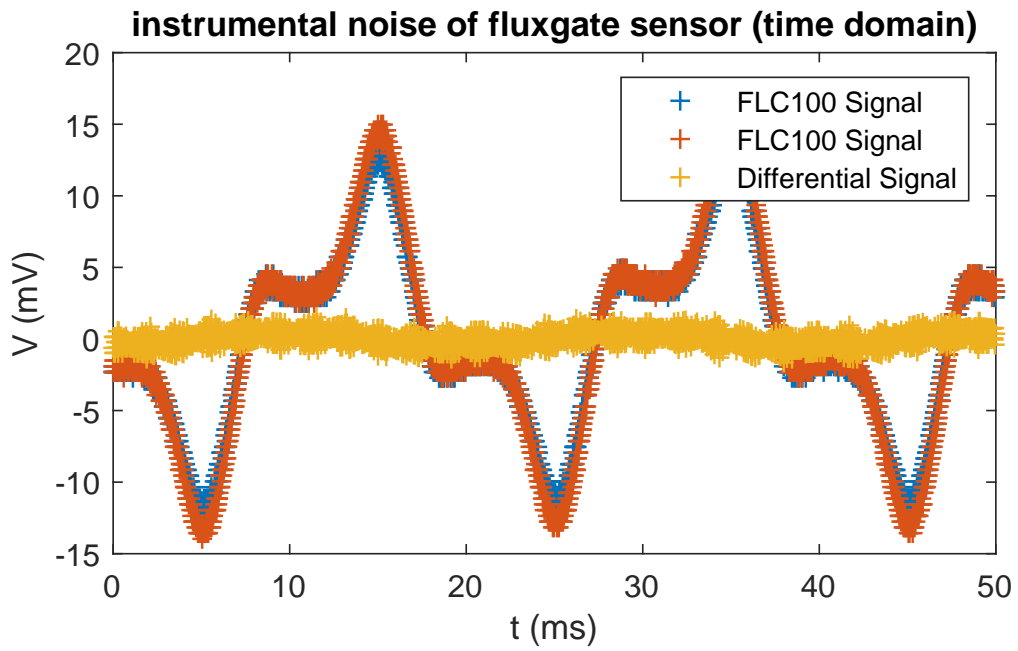


Figure A.1: In red and blue the measured signals of the fluxgate magnetometers. In yellow the difference between the two measured signals where a scaling factor α has been taken into account.

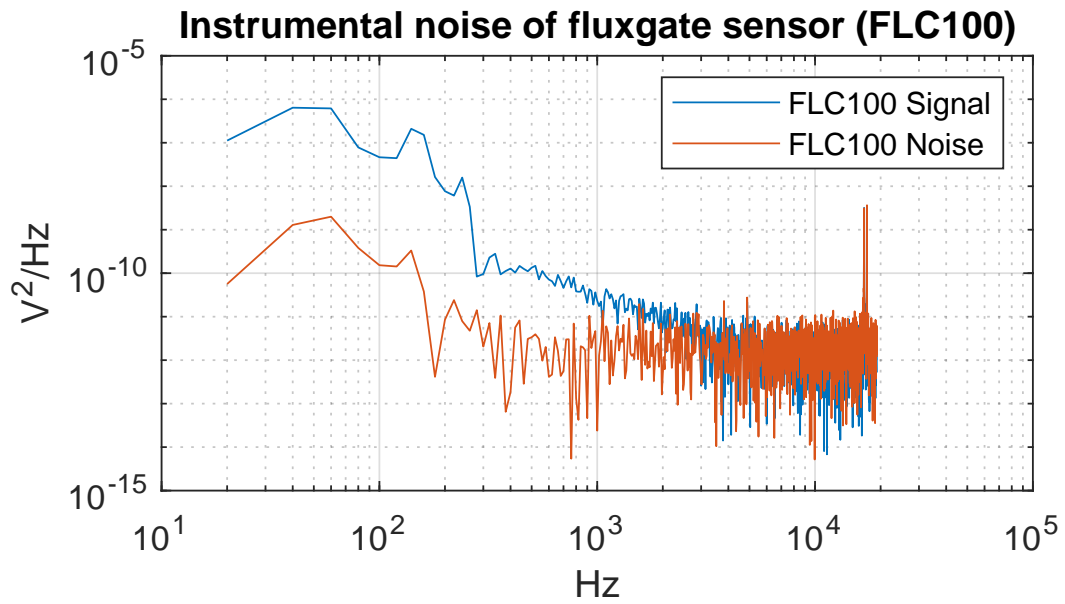


Figure A.2: Calculated spectral density of the measured fluxgate signal in blue and the difference of two magnetic fluxgate sensors in red.

Acknowledgements

Zu aller erst, möchte ich mich bei Professor Meschede für die Möglichkeit bedanken, Teil eines spannenden Projektes zu werden. Durch ihr Vertrauen, konnte ich mich in vielfältiger Weise weiterbilden und eine Forschungsarbeit in der faszinierenden Welt der Quantenphysik durchführen sowie Teil eines internationalen wissenschaftlichen Teams werden.

Darüber hinaus möchte Ich mich bei Professor Stellmer bedanken, für die unkomplizierte Übernahme der Zweitkorrektur meiner Arbeit.

Insbesondere möchte ich mich bei Dr. Alberti bedanken, für einen schier unendlichen Einfallsreichtum in der Problemlösung und dem Auftun interessanter Fragestellungen, sowie für eine ständige Erreichbarkeit und Hilfsbereitschaft. Aber auch für ein angenehmes Betreuungsverhältnis, was zu viel Spaß und Freude während der Zeit meiner Masterarbeit beigetragen hat.

Bei Dr. Alt möchte ich mich für seine zu jeder Zeit bereit stehende Hilfsbereitschaft bedanken und für eine außergewöhnliche Intuition im Aufspüren und Lösen von physikalischen Problemen. I would like to especially thank Manolo who was always there to have fruitful discussions about any problem and offered help at any point.

I would like to thank all members of the meschede group, who have always been willing to share or listen to physical problems and help finding solutions. It have been many fruitful discussions about physics and beyond, which have made working in this group very enjoyable.

Bei meinen Eltern möchte Ich mich bedanken, dass Sie mich zu jeder Zeit unterstützt haben und mit erstaunlicher Ruhe mir in meiner Entwicklung beigestanden haben.

Ich möchte mich bei meiner Freundin bedanken, dafür dass Sie mich zu jeder Zeit mit Rat und Tat unterstützt hat. Du hast für Ablenkung und Erholung, in der doch manchmal anstrengenden Zeit gesorgt hat.

